Aalto University
School of Science

Electromagnetic correlation imaging: image quality and the degree of polarisation

Henri Kellock

Aalto University
School of Science
Department of Applied Physics
Optics and Photonics

Aalto University
School of Science

Abstract of Licentiate Thesis

Author

Henri Kellock

Title of Thesis

Electromagnetic correlation imaging: image quality and the degree of polarisation

Abstract

Image quality of various correlation imaging setups is investigated while taking into account the electromagnetic nature of light, especially the degree of polarisation.

Classical ghost imaging with vectorial light, or electromagnetic correlation imaging, is a 21st century imaging method that can be applied to situations where conventional, direct imaging methods are not possible. This novel imaging method is based on the statistical nature of the light source which is followed by an inherent image quality disadvantage compared to conventional imaging methods. The degree of polarisation of the source has an effect on the image quality, as does the exact arrangement of the setup. Various configurations with two, three or more paths that light originating from a common source takes before it is detected and the image is formed through correlation calculations are explored.

Powerful methods for analysing various setups are presented, such as the concept of the fictitious plane of the effective source, and both analytical and computational methods for efficiently calculating higher-order correlations. It is found that while increasing the degree of polarisation of the source or the number of paths taken enhances the image quality when measured by certain parameters, it decreases the image quality when assessing the result using other image quality parameters. The results of this work can be used to analyse more specific studies and to help improve their image quality.

Research field	Key words
Theoretical optics	**correlation imaging, ghost imaging**
Supervising professor	**Pages**
Matti Kaivola	**67**
Thesis advisor	**Language**
Andriy Shevchenko	**English**
Thesis examiner	**Date**
Sergei Tretyakov	**22.4.2018**

☒ **The thesis can be read at https://aaltodoc.aalto.fi/handle/123456789/27**

Aalto-yliopisto
Perustieteiden korkeakoulu

Lisensiaatintutkimuksen tiivistelmä

Tekijä

Henri Kellock

Lisensiaatintutkimuksen nimi

Kuvanlaatu ja polarisaatioaste elektromagneettisessa korrelaatiokuvauksessa

Tiivistelmä

Erilaisten korrelaatiokuvausasetelmien kuvanlaatua tutkitaan ottaen huomioon valon elektromagneettisen luonteen, erityisesti polarisaatioasteen.

Klassinen haamukuvaus vektoriaalisella valolla, toiselta nimeltään elektromagneettinen korrelaatiokuvaus, on 2000-luvun kuvantamismenetelmä, jota voidaan käyttää tilanteissa joissa perinteiset, suorat kuvantamismenetelmät eivät ole mahdollisia. Klassinen korrelaatiokuvaus perustuu valonlähteen epädeterministiseen statistiikkaan, joka johtaa huonompaan kuvanlaatuun verrattuna perinteisiin kuvantamismetodeihin. Lähteen polarisaatioaste ja kuvausastelmien yksityiskohdat vaikuttavat kuvanlaatuun. Tutkittavana ovat useat kuvausastelmat, joissa yhteisestä lähteestä peräisin oleva valo kulkee kahta, kolmea tai useampaa haaraa pitkin kunnes valo osuu ilmaisimiin.

Työssä esitellään erilaisia tapoja, joilla tutkittavana olevia kuvausasetelmia voidaan analysoida tehokkaasti. Näitä tapoja ovat efektiivisen lähteen konsepti sekä analyyttisiä ja laskennallisia metodeja korkeamman kertaluvun korrelaatioiden laskemiseen. Sekä polarisaatioasteen että kuvauksen kertaluvun kasvattaminen paransivat kuvanlaatua tietyillä tavoilla kuvanlaatua arvioiden. Samojen parametrien muutokset vaikuttivat päinvastoin kun kuvanlaatua mitattiin toisilla tavoilla. Työn tuloksia voidaan käyttää kun halutaan analysoida tutkinnan alla olevia korrelaatiokuvausasetelmia sekä niiden kuvanlaatua.

Tutkimusala	Avainsanat
Teoreettinen optiikka	**korrelaatiokuvaus, haamukuvaus**
Vastuuprofessori	**Sivumäärä**
Matti Kaivola	**67**
Ohjaaja	**Kieli**
Andriy Shevchenko	**Englanti**
Työn tarkastaja	**Päiväys**
Sergei Tretyakov	**22.4.2018**

☒ **Luettavissa verkossa osoitteessa https://aaltodoc.aalto.fi/handle/123456789/27**

Contents

Nomenclature

BS	beam splitter
CCD	charge-coupled device, common imaging sensor type
CNR	contrast-to-noise ratio
CSDM	the cross-spectral density matrix
DoP	the degree of polarisation
FPES	fictitious plane of the effective source
ICF	intensity correlation function
MCM	mutual coherence matrix
SNR	signal-to-noise ratio

1. Introduction

Conventionally, imaging has focused on gathering information on the object of interest by direct means. For example, light reflecting from or transmitting through the object is gathered with a lens or mirror system directly into a camera. Depending on the configuration of the optical components, an image or a Fourier transform of the object can be found when specific conditions are met [1]. All modern consumer cameras follow various recipes of this basic principle, from the first film cameras to 50-megapixel digital single lens reflex cameras and from minuscule smartphone cameras to multi-metre-wide telescopes.

In 1995, an alternative to these direct imaging methods was introduced in the form of ghost imaging and diffraction [2, 3]. These methods rely on entangled photons of which the first traverses the object and is detected by a bucket detector and the other part of the pair is imaged with a spatially-sensitive camera. The data from either detector on its own is not enough to form a picture, but when the information is combined, the image of the object can be inferred through coincidence counts between the detectors. This permits imaging in situations where it was not conventionally possible.

As suggested in the original paper [2], it is possible to observe this same phenomenon using classical light. The first demonstration using classical light came in 2002 [4]. Entangled photons were replaced by laser beams that were angularly correlated; when one beam moved to the left, so did the other. Again, the first beam traversed through the object into a bucket detector and the second was imaged by a CCD camera. The image of the object could only be formed through the correlation of the two signals.

Another setup, although similar to the 2002 setup in the sense that it relied on classical light, was practically very different when the light source was changed into a pseudothermal one. Introduced in theory in 2004 and in practice a year later [5–7], in this case the source consisted of a laser, a rotating

ground glass disk and a beam splitter that were used to produce two mutually correlated but individually spatially incoherent light fields. One beam propagated into the reference arm where the intensity distribution was measured and the other into the test arm where the object was located together with a bucket detector. Depicted in figure 1.1, the image is formed in the correlator which is connected to both detectors.

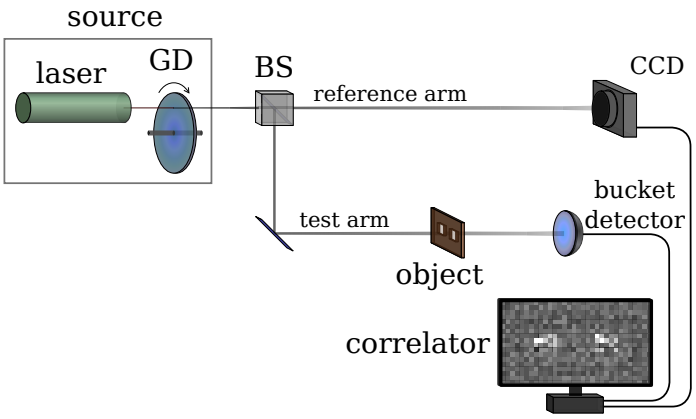

Figure 1.1. A typical classical ghost imaging setup consists of a source and a beam splitter (BS) from which identical light fields propagate into the reference and test arms. The source commonly consists of a laser and a rotating ground glass disk (GD) that produce a pseudothermal random light . The reference arm has the CCD camera while the test arm has the object and a bucket detector. The individual detectors are not enough but combining the information from both detectors in a correlator helps form an image of the object.

The use of pseudothermal light had the advantage of readily available, bright sources, while the disadvantage was poor visibility. This sparked many studies on methods to improve the visibility and other parameters related to the quality of the resulting ghost image [5, 8].

Although many situations can be reduced to the study of scalar fields, light is fundamentally an electromagnetic field with vectorial properties. Based on Maxwell's equations, classical optical coherence theory is used to study these fields [9, 10]. Taking into account the vectorial nature of light not only enables us to study the effects on image quality [11–15], but also applications that require knowledge of all components of the light field [16, 17].

The main objective of this thesis is to study ghost imaging from the viewpoint of the electromagnetic nature of light and especially concentrate on image quality and the degree of polarisation. When on the subject of image quality, we consider setups with multiple arms and assess the affect higher-order correlations have.

This work begins with a brief background introduction of electromagnetic fields, random processes, coherence theory, intensity correlations and Jones calculus in chapter 2. In chapter 3 we introduce some preliminary concepts of

ghost imaging, including propagation laws, the concept of an effective source and the conditions for both ghost imaging and ghost diffraction. Chapter 4 begins with an introduction to the second- and higher-order setups that are to be analysed and then concentrates on assessing the image quality of these setups as a function of the degree of polarisation.

2. Electromagnetic correlations

In this chapter we cover essential theory used when studying ghost imaging with pseudothermal random light. We begin with electromagnetic fields and continue to random processes before going into optical coherence theory, the foundation of the study of light fluctuations. Separate sections are given to intensity correlations and Jones calculus, since these are of key importance for the image quality and applications studied in this thesis.

2.1 Electromagnetic fields

As classical correlation imaging is fundamentally a study of light, an electromagnetic field, we use Maxwell's equations to study the properties of this field.

2.1.1 Maxwell's equations

In the space–time domain the Maxwell's equations are[1] [18]

$$\nabla \cdot \mathbf{D}(\mathbf{r}, t) = \rho(\mathbf{r}, t), \tag{2.1a}$$

$$\nabla \cdot \mathbf{B}(\mathbf{r}, t) = 0, \tag{2.1b}$$

$$\nabla \times \mathbf{E}(\mathbf{r}, t) = -\partial_t \mathbf{B}(\mathbf{r}, t), \tag{2.1c}$$

$$\nabla \times \mathbf{H}(\mathbf{r}, t) = \partial_t \mathbf{D}(\mathbf{r}, t) + \mathbf{j}(\mathbf{r}, t), \tag{2.1d}$$

where $\mathbf{D}$ is the electric displacement, $\mathbf{E}$ is the electric field, $\mathbf{B}$ is the magnetic flux density, $\mathbf{H}$ is the magnetic field. The free charge and current densities are respectively ρ and $\mathbf{j}$.

In certain applications it is easier to analyse the problem in the space–frequency domain. To switch between equations in the space–time and space–frequency

[1] Here I use the abbreviation $\partial_t \equiv \partial/\partial t$.

domain we use the Fourier transform pair [19]

$$\tilde{\mathbf{F}}(\mathbf{r},\omega) = \frac{1}{\sqrt{2\pi}} \int_{-\infty}^{\infty} \mathbf{F}(\mathbf{r},t) e^{i\omega t} \mathrm{d}t, \tag{2.2a}$$

$$\mathbf{F}(\mathbf{r},t) = \frac{1}{\sqrt{2\pi}} \int_{-\infty}^{\infty} \tilde{\mathbf{F}}(\mathbf{r},\omega) e^{-i\omega t} \mathrm{d}\omega, \tag{2.2b}$$

where $\tilde{\mathbf{F}}(\mathbf{r},\omega)$ is the Fourier transform (or Fourier spectrum) of $\mathbf{F}(\mathbf{r},t)$.

Using equations (2.1) and (2.2b) we obtain Maxwell's equations in the space–frequency domain as

$$\nabla \cdot \tilde{\mathbf{D}}(\mathbf{r},\omega) = \tilde{\rho}(\mathbf{r},\omega), \tag{2.3a}$$

$$\nabla \cdot \tilde{\mathbf{B}}(\mathbf{r},\omega) = 0, \tag{2.3b}$$

$$\nabla \times \tilde{\mathbf{E}}(\mathbf{r},\omega) = i\omega \tilde{\mathbf{B}}(\mathbf{r},\omega), \tag{2.3c}$$

$$\nabla \times \tilde{\mathbf{H}}(\mathbf{r},\omega) = -i\omega \tilde{\mathbf{D}}(\mathbf{r},\omega) + \tilde{\mathbf{j}}(\mathbf{r},\omega). \tag{2.3d}$$

These equations hold separately for all the angular frequencies of the space–time domain field.

2.1.2 Response of matter

In the space–frequency domain the constitutive relations governing the response of a linear, isotropic, homogeneous and spatially nondispersive medium are [10]

$$\tilde{\mathbf{D}}(\mathbf{r},\omega) = \epsilon(\omega) \tilde{\mathbf{E}}(\mathbf{r},\omega), \tag{2.4a}$$

$$\tilde{\mathbf{B}}(\mathbf{r},\omega) = \mu(\omega) \tilde{\mathbf{H}}(\mathbf{r},\omega), \tag{2.4b}$$

where $\epsilon(\omega)$ is the electric permittivity and $\mu(\omega)$ is the magnetic permeability.

2.1.3 Wave equation

Most of the light propagation in classical ghost imaging setups happens either in free space or in a dielectric medium. In both cases there are no free charges $\tilde{\rho}(\mathbf{r},\omega) = 0$ or currents $\tilde{\mathbf{j}}(\mathbf{r},\omega) = \mathbf{0}$. Taking the curl of equation (2.3c) and using equations (2.3a), (2.3d), and (2.4) together with the identity $\nabla \times (\nabla \times \mathbf{A}) = \nabla(\nabla \cdot \mathbf{A}) - \nabla^2 \mathbf{A}$, we acquire the Helmholtz equation for the electric field

$$\left(\nabla^2 + k^2\right) \tilde{\mathbf{E}}(\mathbf{r},\omega) = 0, \tag{2.5}$$

where the wave number is $k \equiv \omega\sqrt{\epsilon(\omega)\mu(\omega)}$. Due to the high frequency of light, the magnetic polarisation of media does not play an important part in most phenomena. Therefore it is enough to consider the electric part of the electromagnetic field.

2.2 Random processes

Random processes are an essential part of ghost imaging with pseudothermal light and of statistical optics in general. Although not all, many light sources rely on emissions from a very large amount of atoms or other sources of uncertainty such as uneven surfaces or turbulent fluids [10]. Although the underlying statistical nature of the processes that generate the light might be very different, the central limit theorem states that they tend towards Gaussian distributions [9].

Here we introduce some fundamental concepts and then concentrate on those processes which are of the most interest when dealing with pseudothermal light, that is Gaussian random processes.

2.2.1 Fundamental concepts

The random process is a continuous set of random variables and it is denoted by $X(t)$, where $t \in \mathbb{R}$. The random process $X(t)$ does not depend on t deterministically.

For a complete description of the random process the n-fold joint probability density function, $p_n[X_1(t), \ldots, X_n(t)](x_1, \ldots, x_n)$, is needed for all $n \in \mathbb{N}$. However, in practice the first two probability density functions normally suffice. With these we can calculate the expectation or *mean* value

$$\langle X(t) \rangle = \int x p_1[X(t)](x) \mathrm{d}x \tag{2.6}$$

and the cross-correlation function between two processes,

$$\langle X_1(t) X_2(t) \rangle = \iint x_1 x_2 p_2[X_1(t), X_2(t)](x_1, x_2) \mathrm{d}x_1 \mathrm{d}x_2, \tag{2.7}$$

where $X_\alpha(t)$, $\alpha \in \{1, 2\}$, is a continuous random process. For two *complex* random processes, $Z_\alpha(t)$, the definition of the cross-correlation function is [9]

$$\langle Z_1^*(t) Z_2(t) \rangle = \iint z_1^* z_2 p_2[Z_1(t), Z_2(t)](z_1, z_2) \mathrm{d}z_1 \mathrm{d}z_2. \tag{2.8}$$

The *deviation* gives the distance of a single outcome from the mean and is defined as

$$\Delta X(t) \equiv X(t) - \langle X(t) \rangle . \tag{2.9}$$

The width of the probability density function is described by the standard deviation, $\sigma_{\mathrm{N}}[X(t)]$, defined here as

$$\sigma_{\mathrm{N}}[X(t)] \equiv \sqrt{\left\langle [\Delta X(t)]^2 \right\rangle} = \sqrt{\langle X(t)^2 \rangle - \langle X(t) \rangle^2}. \tag{2.10}$$

Physically, this describes the *noise* related to the system described by the random process $X(t)$.

Another way of defining the operator $\langle \ldots \rangle$ is by taking the ensemble over the set of all possible realisations of the random process $\{X^{(k)}(t)\}$. In this case the mean becomes

$$\langle X(t) \rangle = \lim_{K \to \infty} \frac{1}{K} \sum_{k=1}^{K} X^{(k)}(t) \tag{2.11}$$

and it is usually called the *ensemble average* in this form, which is equivalent to the definition in equation (2.6).

2.2.2 Gaussian random processes and the moment theorem

Gaussian random processes play an important role in describing physical phenomena which arrive from a large number of independent additive contributions. Light coming from the sun, an incandescent bulb and a laser shone through a ground glass disk (used in the example configurations in chapter 3) all follow from a large number of independent sources [7, 10].

Although the underlying process for each independent contribution might obey completely different statistics, the central limit theorem states that, when there are enough contributions the sum of them obeys Gaussian statistics [9,19]. Thus in many practical cases the intensity fluctuations of light can be modelled as complex Gaussian random processes. In this case we can use the complex Gaussian moment theorem to express a $2N$-order correlation function in terms of second-order correlation functions as [20]

$$\begin{aligned} &\langle Z_1^*(t_1) \cdots Z_N^*(t_N) Z_{N+1}(t_{N+1}) \cdots Z_{2N}(t_{2N}) \rangle \\ &= \sum_{N!} \left\langle Z_1^*(t_1) \underline{Z_{N+1}(t_{N+1})} \right\rangle \cdots \left\langle Z_N^*(t_N) \underline{Z_{2N}(t_{2N})} \right\rangle , \end{aligned} \tag{2.12}$$

where the summation is performed over the $N!$ different permutations of the underlined terms.

2.2.3 Stationary and ergodic processes

A *strictly stationary* random process has an n-fold probability density function which is time independent for all $n \in \mathbb{N}$. In this case, if t denotes time, all the n time parameters in the n-fold probability density function can be shifted by the same amount without changing the outcome of a measurement related to that random process. For a *wide-sense stationary* random process it is sufficient that the first moment does not depend on t and thus $\langle X(t) \rangle$ is constant in time [10, 20].

All complex Gaussian random processes have the feature that if they are wide-sense stationary, they are also strictly stationary [20]. Thus referring to a stationary process is sufficient when the process has Gaussian statistics.

Ergodic processes have the feature that the time average of any given realisation of the process is equal to the ensemble average of the process at any given time. Mathematically we have

$$\langle X(t)\rangle = \lim_{K\to\infty}\frac{1}{K}\sum_{k=1}^{K} X^{(k)}(t) = \lim_{T\to\infty}\frac{1}{T}\int_{-T/2}^{T/2} X^{(\kappa)}(t')\mathrm{d}t'. \tag{2.13}$$

As the rightmost part of equation (2.13) is time-independent, ergodicity implies that the process is stationary. A sufficient condition for ergodicity of a random process is that the correlations between the realisations disappear sufficiently fast as the time difference between them grows [9].

2.3 Coherence theory

The theory of optical coherence is the study of random fluctuations in electromagnetic fields, and more specifically in light. Here we introduce the mutual coherence matrix (MCM) and cross-spectral density matrix (CSDM) which are used in all studies of the correlations related to classical ghost imaging. Also, we introduce our definition for the degree of polarisation (DoP).

2.3.1 Space–time domain correlations

In electromagnetic ghost imaging we are often interested in the correlation of two (or more) electric field vectors. The correlation information between all the components of two electric field vectors $\mathbf{E}_\alpha$ and $\mathbf{E}_\beta$ is contained in the mutual coherence matrix (MCM)

$$\mathbf{\Gamma}_{\alpha\beta} \equiv \left\langle \mathbf{E}_\alpha^* \mathbf{E}_\beta^{\mathrm{T}} \right\rangle = \begin{pmatrix} \Gamma_{xx,\alpha\beta} & \Gamma_{xy,\alpha\beta} \\ \Gamma_{yx,\alpha\beta} & \Gamma_{yy,\alpha\beta} \end{pmatrix}, \tag{2.14}$$

where $\Gamma_{ij,\alpha\beta} \equiv \langle E_{i,\alpha}^*(t) E_{j,\beta}(t')\rangle$, $i,j \in \{x,y\}$, is the cross-correlation function [see equation (2.8)] between the field components $E_{i,\alpha}$ and $E_{j,\beta}$ of the field vectors $\mathbf{E}_\Omega = [E_{x,\Omega}(t), E_{y,\Omega}(t)]$, $\Omega \in \{\alpha,\beta\}$. The electric fields generally depend on different spatial coordinates, but for notational brevity we only explicitly write them when it is relevant to the analysis. Thus we ask the reader to keep in mind that generally $\mathbf{E}_\Omega \equiv \mathbf{E}_\Omega(\mathbf{r}_\Omega)$ for any Ω that is being treated.

2.3.2 Space–frequency domain correlations

Most of the analysis in this thesis is performed in the frequency domain. The cross-spectral density matrix (CSDM) is defined as

$$\mathbf{W}_{\alpha\beta} \equiv \left\langle \mathbf{E}_\alpha^* \mathbf{E}_\beta^{\mathrm{T}} \right\rangle = \begin{pmatrix} W_{xx,\alpha\beta} & W_{xy,\alpha\beta} \\ W_{yx,\alpha\beta} & W_{yy,\alpha\beta} \end{pmatrix}, \tag{2.15}$$

where $W_{ij,\alpha\beta} \equiv \langle \tilde{E}_{i,\alpha}^*(\omega) \tilde{E}_{j,\beta}(\omega) \rangle$, $i, j \in \{x, y\}$, is the cross-correlation function of the components of the electric field, now in the frequency domain.

Note that, although the space–frequency domain electric field vector, $\mathbf{E}_\Omega = [\tilde{E}_{x,\Omega}(\omega), \tilde{E}_{y,\Omega}(\omega)]$, $\Omega \in \{\alpha, \beta\}$, consists of Fourier transforms of the space–time domain electric field components, $E_{x,\Omega}(t)$ and $E_{y,\Omega}(t)$, we have denoted it with the exact same symbol as the space–time domain electric field vector from section 2.3.1. This is because in most situations it is clear which domain we are in from the context: we are using either the MCM (space–time domain) or CSDM (space–frequency domain). Also, in most situations related to ghost imaging, it does not matter which domain we are in and most results are equivalent in both domains. Especially, there exists a Fourier transform pair such that [9]

$$W_{ij,\alpha\beta}(\omega) = \frac{1}{\sqrt{2\pi}} \int_{-\infty}^{\infty} \Gamma_{ij,\alpha\beta}(t) e^{i\omega t} \mathrm{d}t \tag{2.16a}$$

$$\Gamma_{ij,\alpha\beta}(t) = \frac{1}{\sqrt{2\pi}} \int_{0}^{\infty} W_{ij,\alpha\beta}(\omega) e^{-i\omega t} \mathrm{d}\omega, \tag{2.16b}$$

which ensures that with many results, the MCM and CSDM are interchangeable. If in some case there is a difference between the domains and there is a risk of confusing the two, we will explicitly denote the domain in question.

2.3.3 Degree of polarisation

Considering a stationary, uniformly polarised beam of light moving in the z direction and with the electric field in the xy plane, the polarisation matrix

$$\mathbf{J} \equiv \begin{pmatrix} J_{xx} & J_{xy} \\ J_{yx} & J_{yy} \end{pmatrix}, \tag{2.17}$$

describes the state of polarisation of the beam.

Here $J_{ij} = \langle E_i^* E_j \rangle$, where $i, j \in \{x, y\}$ and the scalar electric fields E_i are the components of a single electric field vector $\mathbf{E} = (E_x, E_y)$. From the definition it follows that

$$J_{ij} = J_{ji}^*, \tag{2.18a}$$

$$J_{ii} \geq 0,\ J_{ii} \in \Re, \tag{2.18b}$$

$$J_{xx}J_{yy} \geq \left|J_{xy}\right|^2, \tag{2.18c}$$

where equation (2.18c) follows from the Schwarz inequality. From equations (2.18b) and (2.18c) we see that $\mathbf{J}$ is Hermitian. The eigenvalues of $\mathbf{J}$ are

$$\begin{aligned}
\lambda_\pm &= \frac{J_{xx}+J_{yy}}{2} \pm \frac{\sqrt{\left(J_{xx}-J_{yy}\right)^2 + 4\left|J_{xy}\right|^2}}{2} \\
&\geq \frac{J_{xx}+J_{yy}}{2} - \frac{\sqrt{\left(J_{xx}-J_{yy}\right)^2 + 4\left|J_{xy}\right|^2}}{2} \\
&\geq \frac{J_{xx}+J_{yy}}{2} - \frac{\sqrt{\left(J_{xx}-J_{yy}\right)^2 + 4J_{xx}J_{yy}}}{2} \\
&= 0,
\end{aligned} \tag{2.19}$$

where the second line follows from $J_{ii} \in \Re$, the third line follows from equation (2.18c). Thus $\mathbf{J}$ is also nonnegative definite and there exists a unitary transformation $\mathbf{U}$ which diagonalises $\mathbf{J}$ so that

$$\mathbf{J}' = \mathbf{U}^\dagger \mathbf{J} \mathbf{U} = \begin{pmatrix} J_1 & 0 \\ 0 & J_2 \end{pmatrix}, \tag{2.20}$$

where $J_1 = \lambda_+ > 0$ and $J_2 = \lambda_-$ are the eigenvalues of $\mathbf{J}$. Since $J_1 \geq J_2$, we may define the degree of polarisation (DoP) as

$$P \equiv \frac{J_1 - J_2}{J_1 + J_2}. \tag{2.21}$$

A mathematically identical definition is given by taking the fully polarised and fully unpolarised parts of the beam and dividing the difference of these intensities by their sum. In light of this, it is intuitive to understand that a completely polarised beam has $P = 1$ while an unpolarised beam has $P = 0$. Partially polarised light has $0 < P < 1$.

Later we will be interested in calculating the trace of the polarisation matrix and especially the relation $\operatorname{tr}\mathbf{J}^n / (\operatorname{tr}\mathbf{J})^n$ will be of interest. Using the invariance of the trace under unitary transformations and the diagonality of $\mathbf{J}'$ we obtain

$$\operatorname{tr}\mathbf{J}^n = J_1^n + J_2^n \tag{2.22a}$$

$$(\operatorname{tr}\mathbf{J})^n = (J_1 + J_2)^n. \tag{2.22b}$$

For later use we define the "trace multiplier" [15]

$$T(P,n) \equiv \frac{\operatorname{tr}\mathbf{J}^n}{(\operatorname{tr}\mathbf{J})^n} = \frac{(1+P)^n + (1-P)^n}{2^n}, \tag{2.23}$$

where the algebraic form is obtained by using equation (2.22).

2.4 Intensity correlations

In ghost imaging the fields are not measured directly but rather the field correlations are found in the intensity correlations. The instantaneous intensity is $I_\alpha(t_\alpha) = \mathbf{E}_\alpha^\dagger(t_\alpha)\mathbf{E}_\alpha(t_\alpha)$ and the measurement gives us the time average of the intensity. We are interested in stationary and ergodic light which has intensity fluctuations [deviation from mean intensity according to equation (2.9), $\Delta I_\alpha(t_\alpha)$] obeying Gaussian statistics. In this case the time average of the intensity is equal to the ensemble average and we can write the intensity measurement as $\langle I_\alpha(t_\alpha)\rangle$.

In the space–frequency domain the intensity is given by the ensemble average $\langle I_\alpha(\omega_\alpha)\rangle$. Due to the Fourier transform relations between the space–time and space–frequency domains in equation (2.16), the results in this section apply to both domains.

The Nth-order intensity correlation function (ICF) is defined as [8, 9]

$$G^{(N)} \equiv \langle I_1 \cdots I_N\rangle = \left\langle \mathbf{E}_1^\dagger \mathbf{E}_1 \cdots \mathbf{E}_N^\dagger \mathbf{E}_N \right\rangle \tag{2.24}$$

and it is normalised as

$$g^{(N)} \equiv \frac{\langle I_1 \cdots I_N\rangle}{\langle I_1\rangle \cdots \langle I_N\rangle}, \tag{2.25}$$

where $N \in \mathbb{Z}$, $N \geq 2$. Each term $\mathbf{E}_\alpha^\dagger \mathbf{E}_\alpha$, $\alpha \in \{1, \ldots, N\}$, in equation (2.24) is a scalar quantity which can be separated into a sum of the intensities in the given basis, i.e., $\mathbf{E}_\alpha^\dagger \mathbf{E}_\alpha = E_{x,\alpha}^* E_{x,\alpha} + E_{y,\alpha}^* E_{y,\alpha} = I_{x,\alpha} + I_{y,\alpha}$ in the orthonormal xy basis. Thus we can write equation (2.24) as

$$G^{(N)} = \sum_{i_1,\ldots,i_N \in \{x,y\}} \langle I_{i_1,1} \cdots I_{i_N,N}\rangle \tag{2.26}$$

Now, let us assume the light fluctuations obey Gaussian statistics. Using the Gaussian moment theorem from equation (2.12), we obtain

$$G^{(N)} = \sum_{i_1,\ldots,i_N \in \{x,y\}} \sum_{N!} \left\langle E_{i_1,1}^* \underline{E_{i_1,1}} \right\rangle \cdots \left\langle E_{i_N,N}^* \underline{E_{i_N,N}} \right\rangle, \tag{2.27}$$

where again the sum is performed while permuting the underlined fields.

We can write the ICFs in their respective domains using traces of the MCMs or CSDMs defined in equations (2.14) and (2.15). For example in the frequency domain, the double- and triple-intensity correlation functions are

$$G^{(2)} = \operatorname{tr}\mathbf{W}_{11} \operatorname{tr}\mathbf{W}_{22} + \operatorname{tr}\mathbf{W}_{12}^\dagger \mathbf{W}_{12} \tag{2.28}$$

and

$$G^{(3)} = \operatorname{tr}\mathbf{W}_{11} \operatorname{tr}\mathbf{W}_{22} \operatorname{tr}\mathbf{W}_{33} + \operatorname{tr}\mathbf{W}_{33} \operatorname{tr}\mathbf{W}_{12}^\dagger \mathbf{W}_{12} + \operatorname{tr}\mathbf{W}_{22} \operatorname{tr}\mathbf{W}_{13}^\dagger \mathbf{W}_{13}$$

$$+ \operatorname{tr}\mathbf{W}_{11} \operatorname{tr}\mathbf{W}_{23}^{\dagger}\mathbf{W}_{23} + 2\Re\left[\operatorname{tr}\left(\mathbf{W}_{12}\mathbf{W}_{23}\mathbf{W}_{31}\right)\right], \tag{2.29}$$

respectively. More on intensity correlations is found in appendix A.

2.5 Jones calculus

Strictly speaking, the matrix formalism in Jones calculus describes the transmission of vector plane waves through optical elements described with matrices. However, an ensemble of these fully coherent fields can make up a field of any state of polarisation and degree of coherence.

If the input ($\mathbf{E}_{\text{in}}$) electric field vector of a realisation of a random field is transmitted through an optical element then the output is

$$\mathbf{E}_{\text{out}} = \mathbf{T}\mathbf{E}_{\text{in}}, \tag{2.30}$$

where the Jones matrix,

$$\mathbf{T} = \begin{pmatrix} T_{xx} & T_{xy} \\ T_{yx} & T_{yy} \end{pmatrix}, \tag{2.31}$$

with $T_{ij} \in \mathbb{C}$, $i, j \in \{x, y\}$, describes the transmission of the deterministic linear optical element. For later convenience, we define the matrices

$$\mathbf{M}^{ij} \equiv \hat{\mathbf{e}}_i \hat{\mathbf{e}}_j^T, \tag{2.32a}$$

$$\mathbf{T}^{i} \equiv \mathbf{M}^{ii}, \tag{2.32b}$$

$i, j \in \{x, y\}$, where $\hat{\mathbf{e}}_i$ is the unit vector in the i direction. Equation (2.32b) gives the Jones matrix, $\mathbf{T}^i$, of the i polariser, a common physical component which lets the ith component of the light continue through unchanged while blocking the orthogonal component completely.

A system with the optical element $\mathbf{T}$ has the correlation [from equations (2.15) and (2.30)]

$$\mathbf{W}_{\text{out}} = \mathbf{T}^{*}\mathbf{W}_{\text{in}}\mathbf{T}^{\text{T}} \tag{2.33}$$

between the input ($\mathbf{W}_{\text{in}}$) and output ($\mathbf{W}_{\text{out}}$) CSDMs.

3. Classical ghost imaging

Classical ghost imaging, or correlation imaging, is a 21st century imaging method where correlations between the intensity fluctuations of light are used to obtain information on the object in previously unimaginable situations. We skip the consideration of quantum ghost imaging [2, 3] and classically correlated beams [4], and instead focus entirely on correlation imaging with a pseudothermal light source [5–7].

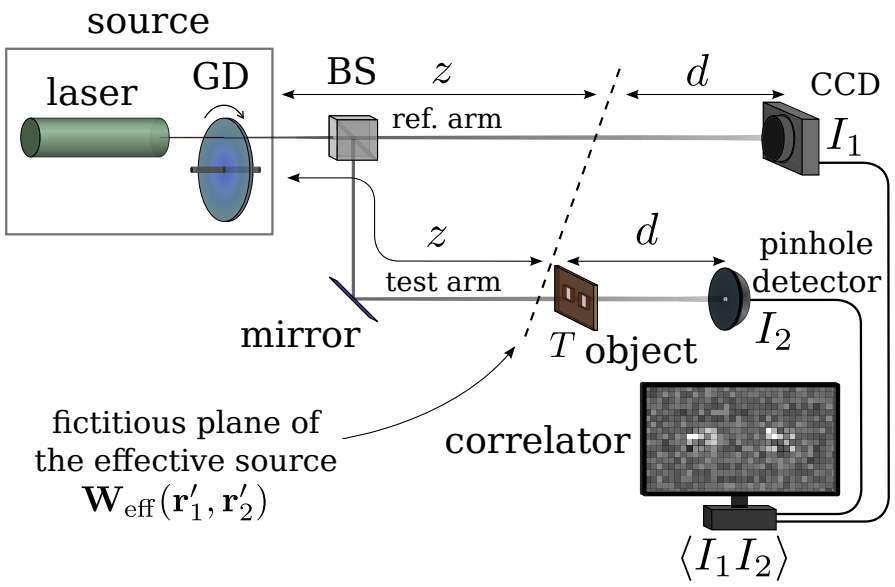

Figure 3.1. A complete ghost imaging setup showing all the main components and the fictitious plane of the effective source. This setup is analysed in parts and the components are explained in detail in later sections. Figure first published in [17].

The basic double-intensity ghost imaging setup to be examined in this chapter is shown in figure 3.1. The main parts of this system to consider are the source, the beam splitter, the object and the detectors, and of course the propagation between the components. The first section of this chapter concentrates on the source and the concept of the effective source, not forgetting the propagation between the planes where these are defined. In sections 3.2 and 3.3 we show how to use lensless correlation imaging to form the image and Fourier transform of the object, respectively. We have kept the analysis in this chapter

as simple as possible and refer to chapter 2 when necessary.

3.1 Preliminaries for ghost imaging

In this section we concentrate on analysing the setup up to the plane of the effective source where the light has travelled an equal amount in both arms from the source (or beam splitter). We begin by considering a spatially completely incoherent source and then we see how the mutual coherence matrix evolves during equal propagation in both arms up until the fictitious plane of the effective source (FPES).

3.1.1 The source

We assume the source to be uniformly polarised source and thus described by the cross-spectral density matrix (CSDM)[1]

$$\mathbf{W}_0(\mathbf{r}_0, \mathbf{r}_0') = \mathbf{J}_0 \gamma(\mathbf{r}_0, \mathbf{r}_0'), \tag{3.1}$$

where $\mathbf{J}_0$ is the polarisation matrix of the source and $\gamma(\mathbf{r}_0, \mathbf{r}_0')$ is the coherence function of the source.

Completely incoherent source A combination of a laser and a rotating ground glass disk, as shown in figure 3.1, can be used to create a spatially completely incoherent source, as long as the detector pixel size and detection frequency are chosen appropriately [21]. In this case, equation (3.1) becomes[2]

$$\mathbf{W}_0(\mathbf{r}_0, \mathbf{r}_0') = \mathbf{J}_0 \delta(\mathbf{r}_0' - \mathbf{r}_0), \tag{3.6}$$

where $\delta(\mathbf{r})$ is the two-dimensional Dirac delta function.

[1] The frequency, or angular frequency (ω), is not shown here or later for brevity. However, not that all the CSDMs are functions of frequency.

[2] The Dirac delta function is defined as a distribution $\delta(x - x_0)$ that satisfies [19, 22]

$$f(x_0) = \int f(x)\delta(x - x_0)\mathrm{d}x \tag{3.2}$$

for continuous functions $f(x)$. In physics it is often represented by the integral

$$\delta(x - x_0) = \frac{1}{2\pi} \int \exp\left[ir(x - x_0)\right] \mathrm{d}r. \tag{3.3}$$

In Cartesian coordinates, the two-dimensional Dirac delta function satisfies [23]

$$\delta(\mathbf{x} - \mathbf{x}_0) = \delta(x - x_0)\delta(y - y_0) \tag{3.4}$$

and thus

$$\delta(\mathbf{x} - \mathbf{x}_0) = \frac{1}{4\pi^2} \int \exp\left[i(\mathbf{x} - \mathbf{x}_0) \cdot \mathbf{r}\right] \mathrm{d}^2 r \tag{3.5}$$

is one possible representation of the two-dimensional Dirac delta function.

Gaussian Schell-model source The completely incoherent source assumption that leads to equation (3.6) is often made to ease the calculations and show what information on the object is obtained in the ideal case. However, for more realistic treatments and to ease with image quality calculations, one can use a Gaussian Schell-model source as given by [24,25]

$$\mathbf{W}_0(\mathbf{r}_0, \mathbf{r}_0') = \mathbf{J}_0 \exp\left[-\frac{\mathbf{r}_0^2 + \mathbf{r}_0'^2}{4\sigma_I^2} - \frac{(\mathbf{r}_0' - \mathbf{r}_0)^2}{2\sigma_g^2}\right], \tag{3.7}$$

where $\exp[-(\mathbf{r}_0^2 + \mathbf{r}_0'^2)/(4\sigma_I^2)]$ is an envelope function with σ_I describing its transverse width of the source and $\mu(\mathbf{r}_0' - \mathbf{r}_0) \equiv \exp[-(\mathbf{r}_0' - \mathbf{r}_0)^2/(2\sigma_g^2)]$ is the complex degree of spatial coherence with σ_g describing the source's transverse coherence width.

3.1.2 Propagation equations

Let us assume a general situation where the field in the initial plane, $\mathbf{E}_0(\mathbf{r}_0)$, is allowed to propagate into several different arms through beam splitters and other optical components. In this case we can use the following propagation equation for finding out the field in the final plane of the ith arm

$$\mathbf{E}_\alpha(\mathbf{r}_\alpha) = \int \mathrm{d}^2 r_0 \mathbf{K}_\alpha(\mathbf{r}_0, \mathbf{r}_\alpha)\mathbf{E}_0(\mathbf{r}_0), \tag{3.8}$$

where the matrix $\mathbf{K}_\alpha(\mathbf{r}_0, \mathbf{r}_\alpha)$ contains all the transmission functions for describing the propagation and transformation of the electromagnetic field components from the initial to the ith final plane. Using equation (3.8), we obtain the CSDM between the ith and jth arm as

$$\mathbf{W}_{\alpha\beta}(\mathbf{r}_\alpha, \mathbf{r}_\beta) = \iint_{-\infty}^{\infty} \mathrm{d}^2 r_0 \mathrm{d}^2 r_0' \mathbf{K}_\alpha^*(\mathbf{r}_0, \mathbf{r}_\alpha)\mathbf{W}_0(\mathbf{r}_0, \mathbf{r}_0')\mathbf{K}_\beta^{\mathrm{T}}(\mathbf{r}_0', \mathbf{r}_\beta), \tag{3.9}$$

where $\mathbf{W}_0(\mathbf{r}_0, \mathbf{r}_0') \equiv \langle \mathbf{E}_0^*(\mathbf{r}_0)\mathbf{E}_0^{\mathrm{T}}(\mathbf{r}_0')\rangle$ and $\mathbf{W}_{\alpha\beta}(\mathbf{r}_\alpha, \mathbf{r}_\beta) \equiv \langle \mathbf{E}_\alpha^*(\mathbf{r}_\alpha)\mathbf{E}_\beta^{\mathrm{T}}(\mathbf{r}_\beta)\rangle$ are the CSDMs in the initial and final plane, respectively, and the (matrix) kernels $\mathbf{K}_\alpha(\mathbf{r}_0, \mathbf{r}_\alpha)$ and $\mathbf{K}_\beta(\mathbf{r}_0', \mathbf{r}_\beta)$ describe the propagation in their respective arms.

In general, the components of the electromagnetic field may propagate according to their respective transmission functions, or impulse response functions, which are contained in $\mathbf{K}_\alpha(\mathbf{r}_0, \mathbf{r}_\alpha)$. If the only polarisation-dependent optical element, $\mathbf{T}$, is located at a single plane and the light propagation in the system is otherwise described by $K_\alpha(\mathbf{r}_0, \mathbf{r}_\alpha)$, then $\mathbf{K}_\alpha(\mathbf{r}_0, \mathbf{r}_\alpha) = \mathbf{T}K_\alpha(\mathbf{r}_0, \mathbf{r}_\alpha)$. Furthermore, if the light propagates in free space under the paraxial approximation, the impulse response function is [22]

$$K_z(\mathbf{r}_0, \mathbf{r}_\alpha) = \frac{ik}{2\pi z} \exp\left[\frac{ik}{2z}(\mathbf{r}_\alpha - \mathbf{r}_0)^2\right], \tag{3.10}$$

where k is the wave number and z is the propagation distance.

3.1.3 The effective source

In [17] we introduced the concept of the effective source which can be used to simplify calculations in correlation imaging. The basic idea, illustrated in figure 3.2, is to look at a fictitious plane which is located at a distance z from the actual source and define the CSDM of this plane as the effective source. This plane can be shared among multiple arms when a beam splitter is used. Although not a physical entity in the common sense, the effective source shares some properties with the original source. For example, the fields located in the *reference arm* and the *test arm* have the same statistical nature and equivalent spatial distributions as long as they are on the plane of same the effective source.

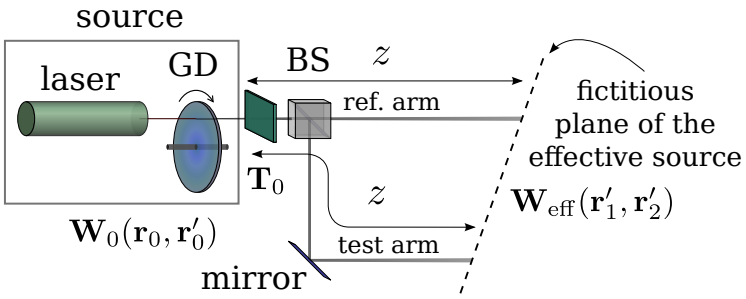

Figure 3.2. A laser and a rotating ground glass disk (GD) are used to create a spatially incoherent source. The beam splitter (BS) separates the light into the reference arm and the test arm. The beam propagates the distance z in both arms to the fictitious plane where the effective source is located [$\mathbf{W}_{\text{eff}}(\mathbf{r}'_1, \mathbf{r}'_2)$]. Figure first published in [17].

Let us examine the situation in figure 3.2 more carefully. The source is characterised by the CSDM $\mathbf{W}_0(\mathbf{r}_0, \mathbf{r}'_0)$ and it is followed by an optical element $\mathbf{T}_0$. After traversing through $\mathbf{T}_0$, the beam is split into two arms, where it propagates the same distance, for a total distance of z from the actual source. We define the CSDM at this plane as the effective source $\mathbf{W}_{\text{eff}}(\mathbf{r}'_1, \mathbf{r}'_2)$. Using equation (3.9) with the kernels $\mathbf{K}_\alpha(\mathbf{r}_0, \mathbf{r}'_\alpha) = \mathbf{T}_0 K_z(\mathbf{r}_0, \mathbf{r}'_\alpha)$, $\alpha \in \{1, 2\}$, we obtain

$$\mathbf{W}_{\text{eff}}(\mathbf{r}'_1, \mathbf{r}'_2) = \iint_{-\infty}^{\infty} \mathrm{d}^2 r_0 \mathrm{d}^2 r'_0 \mathbf{T}_0^* \mathbf{W}_0(\mathbf{r}_0, \mathbf{r}'_0) \mathbf{T}_0^{\mathrm{T}} K_z^*(\mathbf{r}_0, \mathbf{r}'_1) K_z(\mathbf{r}'_0, \mathbf{r}'_2) \tag{3.11}$$

and, when combining with equation (3.10), the form

$$\mathbf{W}_{\text{eff}}(\mathbf{r}'_1, \mathbf{r}'_2) = \frac{k^2}{4\pi^2 z^2} \iint_{-\infty}^{\infty} \mathrm{d}^2 r_0 \mathrm{d}^2 r'_0 \mathbf{T}_0^* \mathbf{W}_0(\mathbf{r}_0, \mathbf{r}'_0) \mathbf{T}_0^{\mathrm{T}}$$

$$\times \exp\left\{\frac{ik}{2z}\left[\left(\mathbf{r}_2' - \mathbf{r}_0'\right)^2 - \left(\mathbf{r}_1' - \mathbf{r}_0\right)^2\right]\right\} \tag{3.12}$$

is reached.

Completely incoherent source Inserting equation (3.6) into equation (3.12) and integrating over $\mathbf{r}_0'$ we have

$$\mathbf{W}_{\text{eff}}(\mathbf{r}_1', \mathbf{r}_2') = \mathbf{J}_{\text{eff}} \frac{k^2}{z^2} e^{ik\left(\mathbf{r}_2'^2 - \mathbf{r}_1'^2\right)/2z} \delta\left[\frac{k}{z}\left(\mathbf{r}_1' - \mathbf{r}_2'\right)\right],$$

where $\mathbf{J}_{\text{eff}} \equiv \mathbf{T}_0^* \mathbf{J}_0 \mathbf{T}_0^{\mathrm{T}}$ and we used equation (3.5) to replace the integral with the Dirac delta function. By appropriately scaling the delta function and removing the inessential phase factor we have the result [17]

$$\mathbf{W}_{\text{eff}}(\mathbf{r}_1', \mathbf{r}_2') = \mathbf{J}_{\text{eff}} \delta(\mathbf{r}_1' - \mathbf{r}_2'), \tag{3.13}$$

that is, *the effective source retains its form for a completely incoherent source*. This result makes it considerably simpler to examine many ghost imaging apparatus and we will use it throughout the ghost imaging analyses in this work.

Gaussian-Schell model source Again starting with equation (3.12) and now inserting the CSDM of the Gaussian-Schell model source from equation (3.7) we obtain

$$\begin{aligned}\mathbf{W}_{\text{eff}}(\mathbf{r}_1', \mathbf{r}_2') = \frac{k^2}{4\pi^2 z^2} \iint_{-\infty}^{\infty} \mathrm{d}^2 r_0 \mathrm{d}^2 r_0' \mathbf{T}_0^* \mathbf{J}_0 \exp\left[-\frac{\mathbf{r}_0^2 + \mathbf{r}_0'^2}{4\sigma_I^2} - \frac{\left(\mathbf{r}_0' - \mathbf{r}_0\right)^2}{2\sigma_g^2}\right] \mathbf{T}_0^{\mathrm{T}} \\ \times \exp\left\{\frac{ik}{2z}\left[\left(\mathbf{r}_2' - \mathbf{r}_0'\right)^2 - \left(\mathbf{r}_1' - \mathbf{r}_0\right)^2\right]\right\}.\end{aligned} \tag{3.14}$$

This most general case will lead to a result that is of a slightly different form than the original source, unless further assumptions are made. To simplify the analysis, we take the source to be considerably wide compared to the size of the object, that is, the transverse width is taken to the limit $\sigma_I \to \infty$. In this case equation (3.14) becomes

$$\begin{aligned}\mathbf{W}_{\text{eff}}(\mathbf{r}_1', \mathbf{r}_2') = \frac{k^2 \mathbf{J}_{\text{eff}}}{4\pi^2 z^2} \iint_{-\infty}^{\infty} \mathrm{d}^2 r_0 \mathrm{d}^2 r_0' \\ \times \exp\left\{-\frac{\left(\mathbf{r}_0' - \mathbf{r}_0\right)^2}{2\sigma_g^2} + \frac{ik}{2z}\left[\left(\mathbf{r}_2' - \mathbf{r}_0'\right)^2 - \left(\mathbf{r}_1' - \mathbf{r}_0\right)^2\right]\right\}\end{aligned} \tag{3.15}$$

where $\mathbf{J}_{\text{eff}} \equiv \mathbf{T}_0^* \mathbf{J}_0 \mathbf{T}_0^{\mathrm{T}}$. Considering the integral with respect to $\mathbf{r}_0$, we can use the common result related to bivariate complex Gaussian integrals[3] to obtain

$$\int_{-\infty}^{\infty} \mathrm{d}^2 r_0 \exp\left[-\left(\frac{1}{2\sigma_g^2} + \frac{ik}{2z}\right)\mathbf{r}_0^2 + \left(\frac{\mathbf{r}_0'}{\sigma_g^2} + \frac{ik}{z}\mathbf{r}_1'\right) \cdot \mathbf{r}_0\right] = \frac{\pi}{a} \exp\left(\frac{\mathbf{b}^2}{4a}\right),$$

[3] It can be shown that

$$\int_{-\infty}^{\infty} \mathrm{d}x \exp\left[-ax^2 + bx\right] = \sqrt{\frac{\pi}{a}} \exp\left[\frac{b^2}{4a}\right],$$

where

$$\mathbf{b} = \frac{\mathbf{r}_0'}{\sigma_g^2} + \frac{ik}{z}\mathbf{r}_1',$$
$$a = \frac{1}{2\sigma_g^2} + \frac{ik}{2z},$$

with $\Re(a) > 0$. Thus equation (3.15) becomes

$$\mathbf{W}_{\text{eff}}(\mathbf{r}_1', \mathbf{r}_2') = \frac{k^2 \mathbf{J}_{\text{eff}}}{4\pi z^2 a} \int_{-\infty}^{\infty} \mathrm{d}^2 r_0' \exp\left[\frac{\left(\frac{\mathbf{r}_0'}{\sigma_g^2} + \frac{ik}{z}\mathbf{r}_1'\right)^2}{4a} - \frac{\mathbf{r}_0'^2}{2\sigma_g^2} + \frac{ik}{2z}\left(\mathbf{r}_0'^2 - 2\mathbf{r}_2' \cdot \mathbf{r}_0'\right)\right]$$
$$\times \exp\left[\frac{ik}{2z}\left(\mathbf{r}_2'^2 - \mathbf{r}_1'^2\right)\right].$$

Now, considering the remaining integral, we have

$$\int_{-\infty}^{\infty} \mathrm{d}^2 r_0' \exp\left[-\left(\frac{1}{2\sigma_g^2} - \frac{ik}{2z} - \frac{1}{4\sigma_g^4 a}\right)\mathbf{r}_0'^2 + \frac{ik}{z}\left(\frac{\mathbf{r}_1'}{2\sigma_g^2 a} - \mathbf{r}_2'\right) \cdot \mathbf{r}_0'\right]$$
$$= \frac{\pi}{a'} \exp\left(\frac{\mathbf{b}'^2}{4a'}\right),$$

where

$$\mathbf{b}' = \frac{ik}{z}\left(\frac{\mathbf{r}_1'}{2\sigma_g^2 a} - \mathbf{r}_2'\right),$$
$$a' = a^* - \frac{1}{4\sigma_g^4 a} = \frac{k^2 \sigma_g^4 a^*}{z^2 + k^2 \sigma_g^4}$$

The last form of a' follows from $|a|^2 = {}^1/_{4\sigma_g^4} + {}^{k^2}/_{4z^2}$ and makes it evident that $\Re(a') > 0$. Using the result of the second integral, the CSDM becomes

$$\mathbf{W}_{\text{eff}}(\mathbf{r}_1', \mathbf{r}_2') = \frac{k^2 \mathbf{J}_{\text{eff}}}{4z^2 a a'} \exp\left[\frac{\mathbf{b}'^2}{4a'} - \frac{k^2 \mathbf{r}_1'^2}{4z^2 a} + \frac{ik}{2z}\left(\mathbf{r}_2'^2 - \mathbf{r}_1'^2\right)\right]. \tag{3.16}$$

Considering the subtraction of two terms in the exponent we may write

$$\frac{\mathbf{b}'^2}{4a'} - \frac{k^2 \mathbf{r}_1'^2}{4z^2 a} = -\frac{k^2}{4z^2 a'}\left(\frac{\mathbf{r}_1'}{2\sigma_g^2 a} - \mathbf{r}_2'\right)^2 - \frac{k^2 \mathbf{r}_1'^2}{4z^2 a}$$
$$= -\frac{k^2}{4z^2 a a'}\left[a\left(\frac{\mathbf{r}_1'}{2\sigma_g^2 a} - \mathbf{r}_2'\right)^2 + a'\mathbf{r}_1'^2\right]$$
$$= \frac{\mathbf{r}_1' \cdot \mathbf{r}_2'}{\sigma_g^2} - a^* \mathbf{r}_1'^2 - a\mathbf{r}_2'^2$$

for $a, b \in \mathbb{C}$ and $\Re(a) \geq 0$ and $a \neq 0$ [26], although commonly the result is limited to $\Re(a) > 0$. Using this we arrive at the useful result of the bivariate complex Gaussian integral

$$\int_{-\infty}^{\infty} \mathrm{d}^2 r \exp\left[-a\mathbf{r}^2 + \mathbf{b} \cdot \mathbf{r}\right] = \frac{\pi}{a} \exp\left(\frac{\mathbf{b}^2}{4a}\right),$$

where $\mathbf{b} = (b_x, b_y) \in \mathbb{C}^2$, $a \in \mathbb{C}$, $\Re(a) \geq 0$ and $a \neq 0$.

$$= -\frac{1}{2\sigma_g^2}\left(\mathbf{r}_1' - \mathbf{r}_2'\right)^2 + \frac{ik}{2z}\left(\mathbf{r}_1'^2 - \mathbf{r}_2'^2\right),$$

where we used $aa' = |a|^2 - 1/4\sigma_g^4 = k^2/4z^2$. Inserting this into equation (3.16), we are left with

$$\mathbf{W}_{\text{eff}}(\mathbf{r}_1', \mathbf{r}_2') = \mathbf{J}_{\text{eff}} \exp\left[-\frac{1}{2\sigma_g^2}\left(\mathbf{r}_1' - \mathbf{r}_2'\right)^2\right]. \tag{3.17}$$

Comparing this to the original Gaussian-Schell model source from equation (3.7) with $\sigma_I \to \infty$ we note that *the effective source retains its form for a Gaussian-Schell model source when the source width is large enough*.

3.2 Ghost imaging

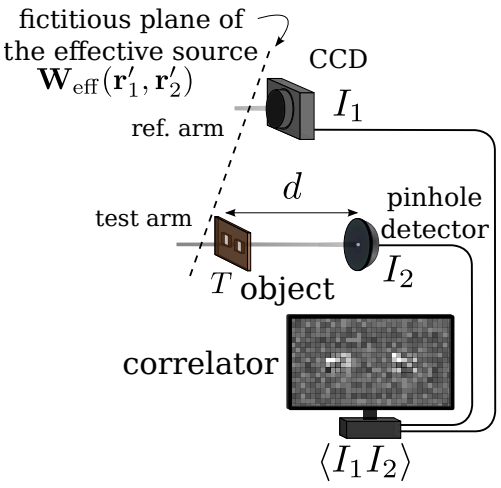

Figure 3.3. In the reference arm the beam is detected straight at the fictitious plane of the effective source [$\mathbf{W}_{\text{eff}}(\mathbf{r}_1', \mathbf{r}_2')$] by a CCD camera ($I_1$). In the test arm the object (T) is located immediately after the effective source and then the beam travels the distance d to the pinhole detector (I_2). The measured intensities are correlated ($\langle I_1 I_2 \rangle$).

Applying the concept of the effective source to ghost imaging, let us examine the simplified, lensless ghost imaging setup shown in figure 3.3. The lens equation for lensless ghost imaging states that the distance to the object and to the reference arm detector must be the same [27]. Thus we can choose the FPES to be immediately in front of the camera and the object in the reference and test arms, respectively. The distance d from the object to the non-resolving test arm detector can be chosen freely and it can either be a pointlike (e.g. pinhole detector, single-pixel detector) or a bucket detector. A pointlike detector has the advantage that it lacks defocusing effects inherent to using a bucket detector [27].

In classical ghost imaging, we simultaneously measure the intensities in the reference arm and the test arm. Taking the ensemble average over a set

of measurement pairs, we can calculate the intensity correlation between the signals in both arms ($\langle I_1 I_2 \rangle$). By disregarding the background ($\langle I_1 \rangle \langle I_2 \rangle$), we obtain the imaging information in the intensity fluctuation correlation ($\langle \Delta I_1 \Delta I_2 \rangle$, where $\Delta I_\alpha = I_\alpha - \langle I_\alpha \rangle$, $\alpha \in \{1, 2\}$). Assuming the fluctuations obey Gaussian statistics, it can be inferred from equation (2.28) while using $\langle I_\alpha \rangle = \operatorname{tr} \mathbf{W}_{\alpha\alpha}$, that the intensity fluctuation correlation is equal to $\operatorname{tr} \mathbf{W}_{12}^\dagger \mathbf{W}_{12}$.

Now, the kernels for the reference and test arm are respectively described by $\mathbf{K}_1(\mathbf{r}_1', \mathbf{r}_1) = \mathbf{I}\delta(\mathbf{r}_1 - \mathbf{r}_1')$ and $\mathbf{K}_2(\mathbf{r}_2', \mathbf{r}_2) = \mathbf{I}T(\mathbf{r}_2')K_d(\mathbf{r}_2', \mathbf{r}_2)$, where $\mathbf{I}$ is the 2×2 unit matrix, $T(\mathbf{r}_2')$ is the transmission function of the (nonpolarising) object. Inserting these kernels into equation (3.9) and integrating over $\mathbf{r}_1'$ we obtain

$$\mathbf{W}_{12}(\mathbf{r}_1, \mathbf{r}_2) = \int_{-\infty}^{\infty} \mathrm{d}^2 r_2' \mathbf{W}_{\mathrm{eff}}(\mathbf{r}_1, \mathbf{r}_2') T(\mathbf{r}_2') K_d(\mathbf{r}_2', \mathbf{r}_2). \tag{3.18}$$

Completely incoherent source Now, if the source is completely incoherent, we can use equation (3.13) for the effective source. After integration with respect to $\mathbf{r}_2'$, the CSDM becomes

$$\mathbf{W}_{12}(\mathbf{r}_1, \mathbf{r}_2) = \mathbf{J}_{\mathrm{eff}} T(\mathbf{r}_1) K_d(\mathbf{r}_1, \mathbf{r}_2). \tag{3.19}$$

The intensity fluctuation correlation can now be expressed as

$$\operatorname{tr} \mathbf{W}_{12}^\dagger \mathbf{W}_{12} = \operatorname{tr} \left(\mathbf{J}_0^\dagger \mathbf{J}_0 \right) \frac{k^2}{4\pi^2 d^2} \left| T(\mathbf{r}_1) \right|^2, \tag{3.20}$$

where we used equation (3.10) for the propagation of distance d and $\mathbf{J}_{\mathrm{eff}} = \mathbf{J}_0$ since there was no polarising elements in front of the source.

Gaussian-Schell model source For an approximation of a slightly more realistic source, the Gaussian-Schell model source with $\sigma_I \to \infty$ can be used. Inserting equation (3.17) into equation (3.18) we obtain

$$\mathbf{W}_{12}(\mathbf{r}_1, \mathbf{r}_2) = \mathbf{J}_{\mathrm{eff}} \int_{-\infty}^{\infty} \mathrm{d}^2 r_2' \exp \left[-\frac{1}{2\sigma_g^2} \left(\mathbf{r}_1 - \mathbf{r}_2' \right)^2 \right] T(\mathbf{r}_2') K_d(\mathbf{r}_2', \mathbf{r}_2). \tag{3.21}$$

Similar to equation (3.20), this becomes

$$\operatorname{tr} \mathbf{W}_{12}^\dagger \mathbf{W}_{12} = \frac{k^2 \operatorname{tr} \left(\mathbf{J}_0^\dagger \mathbf{J}_0 \right)}{4\pi^2 d^2} \left| \int_{-\infty}^{\infty} \mathrm{d}^2 r \exp \left[\frac{ik}{2d} \mathbf{r}^2 - \frac{1}{2\sigma_g^2} \left(\mathbf{r}_1 - \mathbf{r} \right)^2 \right] T(\mathbf{r}) \right|^2 \tag{3.22}$$

upon inserting the free space propagation kernel with the propagation of distance d, $\mathbf{J}_{\mathrm{eff}} = \mathbf{J}_0$ and $\mathbf{r}_2 = \mathbf{0}$. Qualitatively speaking, when the coherence width, σ_g, is extremely small, only the parts of the integral in equation (3.22) close to $T(\mathbf{r}_1)$ survive and the result becomes more similar to equation (3.20) [7]. When the coherence width is larger, the image of the object becomes more blurry. This is discussed in more detail in 4.5.

3.3 Ghost diffraction

In addition to imaging the object, obtaining the object's Fourier transform by ghost imaging techniques has been a major interest, possibly due to the fact that lensless ghost diffraction can be realised accurately with small path lengths from the object to the detector. In lensless ghost diffraction the far field of the object is imaged when both detectors are at the same distance from the source [25, 28–30].

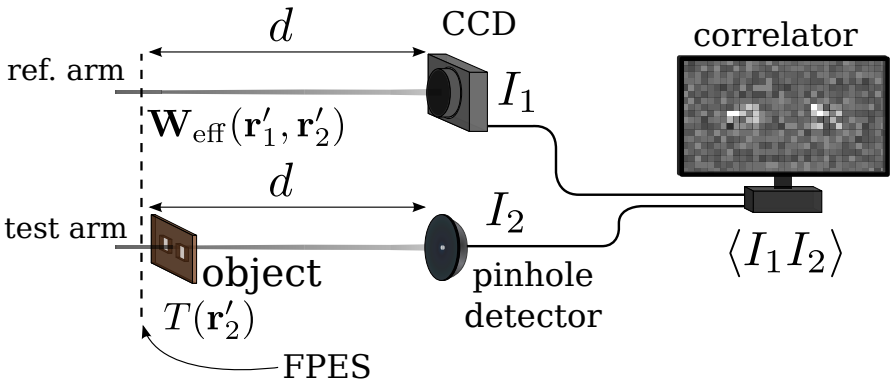

Figure 3.4. In the reference arm the beam propagates the distance d from the fictitious plane of the effective source [$\mathbf{W}_{\text{eff}}(\mathbf{r}_1', \mathbf{r}_2')$] and is detected by a CCD camera (I_1). In the test arm the object (T) is located immediately after the effective source and then the beam travels the distance d to the pinhole detector (I_2). The measured intensities are correlated ($\langle I_1 I_2 \rangle$).

In reference to figure 3.4, we analyse ghost diffraction using the concept of the effective source. As in the previous section, the object is placed immediately after the fictitious plane of the effective source in the test arm, but now both detectors are at the distance d from the FPES in their respective arms. Inserting the kernels $\mathbf{K}_1(\mathbf{r}_1', \mathbf{r}_1) = \mathbf{I}K_{z=d}(\mathbf{r}_1', \mathbf{r}_1)$ and $\mathbf{K}_2(\mathbf{r}_2', \mathbf{r}_2) = \mathbf{I}T(\mathbf{r}_2')K_{z=d}(\mathbf{r}_2', \mathbf{r}_2)$ into equation (3.9) we obtain

$$\mathbf{W}_{12}(\mathbf{r}_1, \mathbf{r}_2) = \iint_{-\infty}^{\infty} \mathrm{d}^2 r_1' \mathrm{d}^2 r_2' \mathbf{W}_{\text{eff}}(\mathbf{r}_1', \mathbf{r}_2') T(\mathbf{r}_2') K_d^*(\mathbf{r}_1', \mathbf{r}_1) K_d(\mathbf{r}_2', \mathbf{r}_2), \tag{3.23}$$

where $T(\mathbf{r}_2')$ is the transmission function of the (nonpolarising) object. Assuming a completely incoherent source and paraxial propagation in the arms we can substitute equations (3.10) and (3.13) into the above CSDM. After integration with respect to $\mathbf{r}_2'$, equation (3.23) can be written as [17]

$$\mathbf{W}_{12}(\mathbf{r}_1, \mathbf{r}_2) = \frac{\mathbf{J}_{\text{eff}} k^2}{2\pi d^2} \exp\left[\frac{ik}{2d}\left(\mathbf{r}_2^2 - \mathbf{r}_1^2\right)\right] \mathcal{F}\left\{T(\mathbf{r}_1')\right\}\left[\frac{k}{d}\left(\mathbf{r}_1 - \mathbf{r}_2\right)\right] \tag{3.24}$$

where

$$\mathcal{F}\left\{T(\mathbf{r})\right\}[\mathbf{k}] = \frac{1}{2\pi} \int_{-\infty}^{\infty} T(\mathbf{r}) \exp\left[i\mathbf{k} \cdot \mathbf{r}\right] \mathrm{d}^2 r \tag{3.25}$$

is the two-dimensional Fourier transform of $T(\mathbf{r})$, normalised similarly to equation (2.2a). Finally, the intensity fluctuation correlation can be expressed as

$$\operatorname{tr} \mathbf{W}_{12}^{\dagger} \mathbf{W}_{12} = \operatorname{tr} \left(\mathbf{J}_0^{\dagger} \mathbf{J}_0 \right) \frac{k^4}{4\pi^2 d^4} \left| \mathcal{F} \left\{ T(\mathbf{r}_1') \right\} \left[\frac{k}{d} \left(\mathbf{r}_1 - \mathbf{r}_2 \right) \right] \right|^2 , \tag{3.26}$$

where again $\mathbf{J}_{\text{eff}} = \mathbf{J}_0$ has been used due to the lack of polarising elements in front of the source.

4. Image quality in higher-order electromagnetic ghost imaging

Since its birth, classical ghost imaging with pseudothermal light has suffered from one obvious weakness when compared to ghost imaging with entangled photons. While the visibility with a quantum source has been high in experiments and is unity in theory, the visibility with a pseudothermal source is limited even in theory [5–7]. Besides visibility [5, 8], other parameters such as signal-to-noise ratio (SNR) [31, 32], contrast-to-noise ratio (CNR) [33] and resolution [7, 8] have been introduced to characterise the image quality in classical ghost imaging.

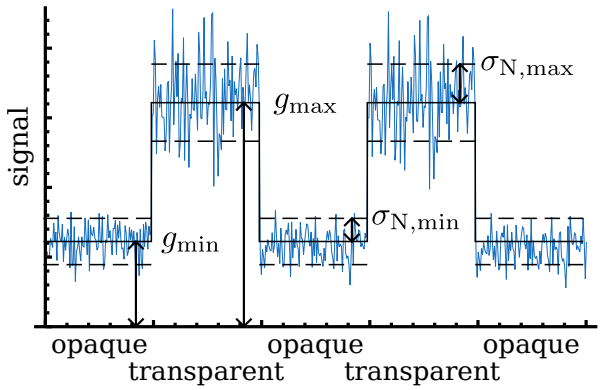

Figure 4.1. A qualitative example realisation of a normalised ghost imaging signal with reduced noise for clarity. The original object that is being imaged has fully transparent and opaque regions. Transparent regions lead to brighter regions in the image and result in the ghost imaging signal $g_{\max}$ with noise $\sigma_{\mathrm{N,max}}$. Opaque regions are not fully dark in the resulting image, but rather exhibit a slightly smaller signal $g_{\min}$ and noise $\sigma_{\mathrm{N,min}}$.

For a qualitative explanation of the image quality problem, we refer to figure 4.1 where an example realisation of the intensity correlation signal is shown. Instead of a one-to-one correspondence between the object and the image, in ghost imaging a fully opaque and a fully transparent region in the object respectively lead to a slightly darker and a slightly brighter area in the image. The average signal (g) and noise (σ_{N}) in the dark area of the image are denoted by the subscript min, while the quantities corresponding to the bright

area of the image are denoted by the subscript max.

The main methods proposed to enhance the image quality have been higher-order intensity correlations [8,11,14,15,34,35], differential ghost imaging [32] and addition of random noise in the case of binary ghost imaging [36]. Also, it has been studied whether it is better to use fully polarised or natural light [11–15].

In this chapter we study the relative absolute maximum image quality of various ghost imaging setups, while varying the degree of polarisation of the source and the imaging order. Section 4.1 is used to introduce the setups we consider when calculating the image quality. In section 4.2 we concentrate on the absolute difference between the dark and bright areas of the image. In section 4.3 we separately assess the noise related to the dark areas of the image and then the noise related to the bright areas. In section 4.4 the CNR combines the information on the contrast and noise to assess the general quality of the image. A brief, qualitative discussion on the subject of the resolution of the resulting image is provided in section 4.5.

4.1 Configurations for correlation imaging

In the ghost imaging setup introduced in section 3.2 there was one reference arm and one test arm, where the test arm contained the object. However, one can add more reference arms and even test arms to the system. The amount of arms in the system defines the order of the intensity correlations. For example, a system with two reference arms and one test arm is a third-order intensity (or triple-intensity) correlation imaging setup. In this section, we introduce ghost imaging setups of different orders in two different cases for each order. In case A the type of arm is not defined and thus imaging information can be in any correlation between the arms. (But the imaging information is never obtained from a single detector's signal.) In case B there is always a single test arm and the rest of the detectors are in reference arms.

As seen in chapter 3 for double-intensity correlation imaging, the imaging information can be calculated from the CSDM, defined by equation (3.9). In chapters 2 and A, higher-order intensity correlations are studied and specifically, it is noted that an arbitrary order intensity correlation function (ICF) can be deconstructed into CSDMs between the arms in the setup.

At this point it is good to make some assumptions on the correlation imaging system to simplify the image quality analysis. We take the source to be a stationary, uniformly polarised beam that has spatial intensity fluctuations

obeying Gaussian statistics. The beam is split into identical copies which continue to different arms in the system. Considering arms α and β, the beam propagates through the imaging systems described by the kernels $K_\alpha(\mathbf{r}', \mathbf{r}_\alpha)$ and $K_\beta(\mathbf{r}', \mathbf{r}_\beta)$ which have no polarisation-altering elements. At the end of the arms the intensities I_α and I_β are detected. Now, using these assumptions, we can insert $\mathbf{W}_0(\mathbf{r}_0, \mathbf{r}_0') = \mathbf{J}_0 \hat{W}_0(\mathbf{r}_0, \mathbf{r}_0')$ and $\mathbf{K}_\Omega(\mathbf{r}_0, \mathbf{r}_\Omega) = \mathbf{I} K_\Omega(\mathbf{r}_0, \mathbf{r}_\Omega)$, $\Omega \in \{\alpha, \beta\}$, into equation (3.9) to obtain [12, 15]

$$\mathbf{W}_{\alpha\beta}(\mathbf{r}_\alpha, \mathbf{r}_\beta) = \mathbf{J}_0 \hat{W}_{\alpha\beta}(\mathbf{r}_\alpha, \mathbf{r}_\beta), \tag{4.1}$$

where

$$\hat{W}_{\alpha\beta}(\mathbf{r}_\alpha, \mathbf{r}_\beta) = \iint_{-\infty}^{\infty} \mathrm{d}^2 r_0 \mathrm{d}^2 r_0' K_\alpha^*(\mathbf{r}_0, \mathbf{r}_\alpha) \hat{W}_0(\mathbf{r}_0, \mathbf{r}_0') K_\beta(\mathbf{r}_0', \mathbf{r}_\beta). \tag{4.2}$$

Assuming $\hat{W}_0(\mathbf{r}_0, \mathbf{r}_0') = \nu(\mathbf{r}_0)\mu(\mathbf{r}_0' - \mathbf{r}_0)\nu(\mathbf{r}_0')$, where ν and μ are both real functions with $\mu(-\mathbf{r}) = \mu(\mathbf{r})$, as is the case for both the completely incoherent source and the Gaussian Schell-model source introduced by equations (3.6) and (3.7), we can write

$$\hat{W}_{\alpha\beta}(\mathbf{r}_\alpha, \mathbf{r}_\beta) = \iint_{-\infty}^{\infty} \mathrm{d}^2 r_0 \mathrm{d}^2 r_0' K_\alpha^*(\mathbf{r}_0, \mathbf{r}_\alpha) \nu(\mathbf{r}_0) \mu(\mathbf{r}_0' - \mathbf{r}_0) \nu(\mathbf{r}_0') K_\beta(\mathbf{r}_0', \mathbf{r}_\beta).$$

Assuming further that $K_\Omega(\mathbf{r}, \mathbf{r}_\Omega)$, $\nu(\mathbf{r})$ and $\mu(\mathbf{r})$ are disconnected with respect to the orthogonal components of the vector $\mathbf{r}$, and by defining,

$$f(\mathbf{r}_0) = K_\alpha(\mathbf{r}_0, \mathbf{r}_\alpha)\nu(\mathbf{r}_0),$$
$$g(\mathbf{r}_0') = K_\beta(\mathbf{r}_0', \mathbf{r}_\beta)\nu(\mathbf{r}_0'),$$

we may use the generalised Schwarz inequality from equation (A.1) to arrive at

$$\left|\hat{W}_{\alpha\beta}(\mathbf{r}_\alpha, \mathbf{r}_\beta)\right|^2 \leq \hat{W}_{\alpha\alpha}(\mathbf{r}_\alpha, \mathbf{r}_\alpha)\hat{W}_{\beta\beta}(\mathbf{r}_\beta, \mathbf{r}_\beta).$$

This leads to

$$0 \leq |\hat{w}_{\alpha\beta}| \leq 1, \tag{4.3}$$

where[1]

$$\hat{w}_{\alpha\beta} \equiv \hat{W}_{\alpha\beta} / \sqrt{\hat{W}_{\alpha\alpha}\hat{W}_{\beta\beta}} \tag{4.4}$$

is the normalised correlation parameter.

[1]The notation of the spatial coordinates, $(\mathbf{r}_\alpha, \mathbf{r}_\beta)$, related to the normalised coordinates of the normalised function $\hat{w}_{\alpha\beta}$ is suppressed for brevity.

In principle, equations (2.23), (2.25), (2.27), (4.1), and (4.4) could be used to write down normalised ICFs for any order in terms of the normalised correlation parameter and DoP. This is done later for the double- and triple-intensity correlation functions, resulting in equations (4.5) and (4.6). Writing down the (normalised) fourth-, fifth- and even sixth-order ICF is still pretty straightforward with their $4! = 24$, $5! = 120$ and $6! = 720$ terms, although admittedly tedious and resulting in lengthy expressions. However, for seventh- and higher-order ICFs ($7! = 5040$ and $N!$ terms in general) this becomes increasingly difficult due to the increased complexity of the higher-order ICFs. There is no known analytical form for the most general case, but we have approached this problem with two different solutions.

First, there exists an analytical form for the minimum and maximum Nth-order ICF for some specific cases. When limiting our analysis to the quality parameters of the extrema of the cases presented shortly, these analytical forms are sufficient to carry out the analysis. The details are relegated to section A.2.

In our second solution, we devised an algorithm to generate a more robust form of the arbitrary-order normalised ICF. The algorithm has some restrictions but it can produce an output with many different parameters that can be adjusted to accommodate for analysing various configurations in addition to the ones that have analytical expressions. The algorithm and its restrictions are discussed in more detail in section A.3.

The explicit mathematical details of both solutions are discussed in the appendix. In 4.1.1, 4.1.2 and 4.1.3 we respectively present the second-, third- and Nth-order intensity correlation configurations to be analysed. For each imaging order we divide our analysis into two classes of correlation imaging setups: in case A the setup is generic and we assume we can obtain maximum information from all of the correlations between the arms, while in case B we assume there is one test arm and $N - 1$ reference arms. In sections 4.2, 4.3 and 4.4 we calculate and compare the quality parameters in the presented configurations.

4.1.1 Double-intensity correlation imaging

Case A: Generic setup In double-intensity correlation imaging the signal is the correlation between the intensities, or mathematically put, the ICF $\langle I_1 I_2 \rangle$. The ICF can be divided into the background, $\langle I_1 \rangle \langle I_2 \rangle = \operatorname{tr} \mathbf{W}_{11} \operatorname{tr} \mathbf{W}_{22}$, and the information-bearing intensity fluctuation correlation, $\langle \Delta I_1 \Delta I_2 \rangle = \operatorname{tr} \mathbf{W}_{12}^{\dagger} \mathbf{W}_{12}$. Employing equations (2.23), (2.24), (2.25), (4.1), and (4.4), the ICF

from equation (2.28) is normalised to

$$g^{(2)}(\mathbf{r}_1, \mathbf{r}_2) = 1 + \frac{P^2 + 1}{2} |\hat{w}_{12}|^2, \tag{4.5}$$

where $\hat{w}_{12}$ is the normalised correlation parameter between the two arms. We can see that in this case the background stays the same independent of the DoP, while the proportion of the information in the signal can be halved by decreasing the DoP from one to zero.

Case B: Specific setup When speaking of case B in double-intensity correlation imaging, the first arm is labelled the reference arm and the second arm is called the test arm; in this case equation (4.5) applies with $\hat{w}_{12}$ being the normalised correlation parameter between the reference and test arm. When speaking of ghost imaging, this parameter is related to the transmission function of the object, and when ghost diffraction is in question it will become proportional to the Fourier transform of the object's transmission function [see sections 3.2 and 3.3, figures 3.3 and 3.4, and equations (3.20) and (3.26)].

Regarding the visibility and other quality parameters, there is no difference between cases A and B. Both cases have the same background and the imaging information is contained in the correlation between the two arms, with the only difference being that in case B they are explicitly labelled as the reference and test arms, respectively.

4.1.2 Triple-intensity correlation imaging

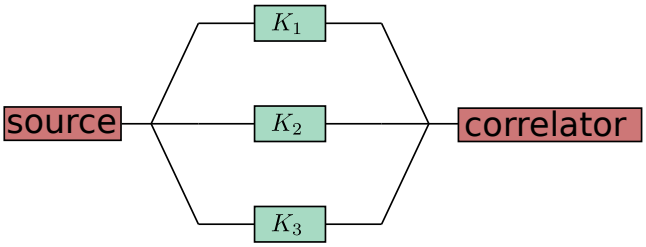

(a) Case A: Generic setup. The light coming from the source is divided into three arms described by the kernels K_α, $\alpha \in \{1, 2, 3\}$. Each arm has an intensity detector from which a signal is passed to the correlator.

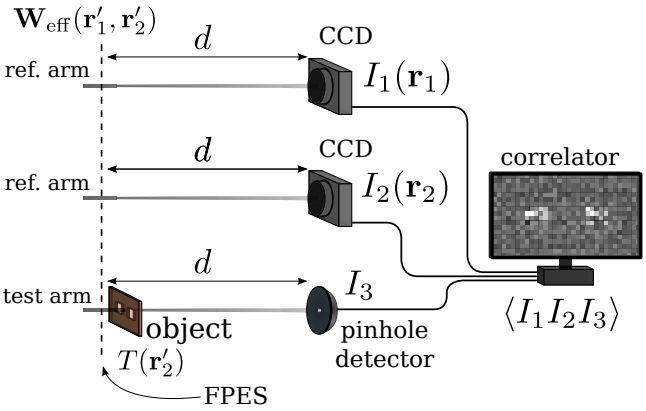

(b) Case B: One test arm, two reference arms. Otherwise similar to the setup in figure 3.4, the ghost diffraction setup illustrated here has two reference arms and one test arm.

Figure 4.2. Triple-intensity correlation imaging setups.

Case A: Generic setup A generic triple-intensity correlation imaging setup is depicted in figure 4.2a. Light from the same source is divided into the three arms described by the kernels K_1 to K_3. At the end of the arms the intensities are detected and correlated.

Employing equations (2.23), (2.24), (2.25), (4.1), and (4.4), the ICF from equation (2.29) is normalised to

$$g_{\mathrm{A}}^{(3)}(\mathbf{r}_1, \mathbf{r}_2, \mathbf{r}_3) = 1 + \frac{P^2+1}{2}\left[|\hat{w}_{12}|^2 + |\hat{w}_{13}|^2 + |\hat{w}_{23}|^2\right] + \frac{3P^2+1}{2}\Re\left[\hat{w}_{12}\hat{w}_{23}\hat{w}_{31}\right], \qquad (4.6)$$

where $\hat{w}_{12}$, $\hat{w}_{13}$ and $\hat{w}_{23}$ are the correlation coefficients containing the information.

Comparing to equation (4.5), the triple-intensity correlation function has proportionally more correlation terms, as the background is similar but there is an increased amount of correlations. As we will see later, this results in

increased visibility.

Case B: One test arm, two reference arms Illustrated in figure 4.2b, the triple-intensity ghost diffraction setup is similar to the second-order setup in figure 3.3, but it has two identical reference arms and one test arm. The normalised ICF is obtained as in the generic triple-intensity case, but now $\hat{w}_{12} = 1$ and $\hat{w}_{13} = \hat{w}_{23}$ due to the static correlation between the identical reference arms [15]. Equation (4.6) becomes

$$g_{\mathrm{B}}^{(3)}(\mathbf{r}_1, \mathbf{r}_1, \mathbf{r}_3) = \frac{P^2 + 3}{2} + \frac{5P^2 + 3}{2} \left|\hat{w}_{13}\right|^2 . \tag{4.7}$$

Note that a triple-intensity ghost imaging setup would have a similar-looking normalised ICF, but the information within $\hat{w}_{13}$ would contain the image of the object, instead of the Fourier transform.

Other setups In our earlier study two slightly different setups were studied [14]. The first one involved one reference arm and two test arms; since it was assumed that also the correlation between the test arms gave information on the object, this case was similar to case A in terms of image quality. The second setup was similar to case B above, but the reference arms were not identical, leaving the correlation parameter open to be adjusted at will.

Cases A and B presented here are the most studied situations and the analysis is restricted to them for simplicity. However, the computational method for calculating the ICFs presented in section A.3 can be used to assess the image quality in various other situations.

4.1.3 Nth-order intensity correlation imaging

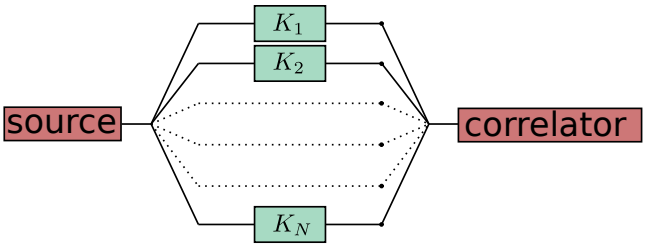

(a) Case A: Generic setup. This setup has a source from which the light is divided into N arms described by the kernels K_α, $\alpha \in \{1, \ldots, N\}$. Each arm has an intensity detector from which a signal is passed to the correlator.

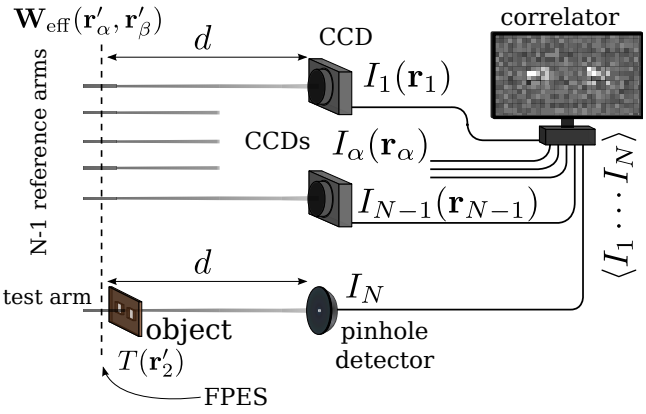

(b) Case B: One test arm, multiple reference arms. Otherwise similar to the setup in figure 3.4, the ghost diffraction setup illustrated here has $N-1$ reference arms and one test arm.

Figure 4.3. Higher-order correlation imaging setups.

Case A: Generic setup A generic Nth-order intensity correlation imaging setup is shown in figure 4.3a. Similar to the triple-intensity case A, there are now N arms and $\triangle(N-1)$ correlation coefficients, where the symbol $\triangle(i)$ denotes the ith triangular number[2].

As mentioned earlier, there is no known analytical form for the normalised Nth-order ICF in terms of the correlation parameters and other describing characteristics, although equations (2.23), (2.25), and (4.1) can in principle be used to find out the ICF of any given order. Our two practical solutions to this problem are introduced in sections A.2 and A.3, and these are sufficient for the image quality analysis presented in sections 4.2, 4.3 and 4.4.

Case B: One test arm, multiple reference arms Similar to the triple-intensity correlation imaging case B, the setup in figure 4.3b has multiple reference arms

[2]The triangular number is defined as $\triangle(i) \equiv i(i+1)/2$ and more on it is explained in section A.3.

and one test arm. Instead of being limited to two reference arms there are now $N-1$ identical reference arms.

As all the correlations between the reference arms contribute to the background, there will be an increased amount of static parts in the normalised Nth-order ICF, however, there will also be more correlations between the test arm and the reference arms.

As in the generic Nth-order setup, there is no known general equation for the normalised Nth-order ICF, but the practical solutions in sections A.2 and A.3 are enough to carry out the image quality analysis later in this chapter.

4.2 Visibility

The visibility of the resulting ghost image has been an important quantity in classical correlation imaging because this is one of the main aspects which separates classical correlation imaging from quantum coincidence imaging [8, 21]. While in quantum ghost imaging the visibility can be close to unity [6], in classical correlation imaging there is always a constant background that will decrease the visibility.

The visibility is used to assess the image contrast, the relative difference between the bright areas of the image when compared to the dark areas. There are two main definitions which have been used for the visibility. The first one was introduced by Gatti *et al.* [21, 37] and was adequate for the study of second-order intensity correlations. It was originally defined as the ratio between the maximum intensity fluctuation correlation and the maximum intensity correlation, mathematically put,

$$V_{\mathrm{G}}^{(2)} \equiv \frac{\langle \Delta I_1 \Delta I_2 \rangle_{\max}}{\langle I_1 I_2 \rangle_{\max}} = \frac{g_{\max}^{(2)} - 1}{g_{\max}^{(2)}}, \tag{4.8}$$

where the latter form follows from the definition of the deviation and the normalised intensity correlation function, that is, from equations (2.9) and (2.25). Another definition for the visibility was introduced later by Cao *et al.* [8] and is similar to the fringe visibility used in interference optics [10]. Unlike the definition given by equation (4.8), the new definition was directly defined for an arbitrary order as

$$V_{\mathrm{C}}^{(N)} \equiv \frac{g_{\max}^{(N)} - g_{\min}^{(N)}}{g_{\max}^{(N)} + g_{\min}^{(N)}}. \tag{4.9}$$

Referring to figure 4.1, the subscript max denotes the transparent part of the object, or the bright part of the image. Likewise, the subscript min denotes the opaque area of the object, or the dark area of the image.

The definition given by equation (4.8) has also been generalised to higher orders. In the work by Liu *et al.* [38] the form

$$V_{\mathrm{G}}^{(N)} = \frac{\left[\langle I_1 \cdots I_N \rangle - \langle I_1 \rangle \cdots \langle I_N \rangle\right]_{\max}}{\langle I_1 \cdots I_N \rangle_{\max}} \tag{4.10}$$

is given. When $N = 2$ it is equal to equation (4.8). The problem with this definition is that it assumes that the background term is always $\langle I_1 \rangle \cdots \langle I_N \rangle$. However, in this thesis the background is generally $\langle I_1 \rangle \cdots \langle I_N \rangle$ only in the generic setup of case A. In other cases, when $N > 2$, the intensity correlation has a larger background, where the correlation between the reference arms adds to the background. For example, if there is one test arm and $N - 1$ reference arms, then the background is $\langle I_1 \rangle \langle I_2 \cdots I_N \rangle$, with the correlation of the reference arms, $\langle I_2 \cdots I_N \rangle$, contributing a constant, visibility-lowering background. Thus, instead of using equation (4.10), we generalise equation (4.8) as

$$V_{\mathrm{G}}^{(N)} = \frac{g_{\max}^{(N)} - g_{\min}^{(N)}}{g_{\max}^{(N)}}, \tag{4.11}$$

to take into account different physical setups.

In the following subsections we will use definitions from equations (4.9) and (4.11) to assess the visibility of different kinds of ghost imaging setups. The main difference between these definitions is the normalisation and we will see that using either definition leads to the same physical interpretations of the image quality in the studied setups. The results are presented as equations and graphs in 4.2.1, 4.2.2 and 4.2.3 while the analysis is relegated to section 4.2.4.

4.2.1 Double-intensity correlation imaging

In double-intensity correlation imaging the imaging information is enclosed in the term $\hat{w}_{12}$ of equation (4.5), regardless of whether a ghost imaging setup (figure 3.3), a ghost diffraction setup (figure 3.4), or a completely generic double-intensity correlation imaging setup is in question.

Using equations (4.5), (4.9), and (4.11) and the extrema provided by equation (4.3) we obtain [11, 12]

$$V_{\mathrm{C}}^{(2)} = \frac{P^2 + 1}{P^2 + 5}, \tag{4.12a}$$

$$V_{\mathrm{G}}^{(2)} = \frac{P^2 + 1}{P^2 + 3}, \tag{4.12b}$$

which are illustrated with the solid lines in figures 4.4 and 4.5, respectively.

4.2.2 Triple-intensity correlation imaging

When moving from double-intensity correlation imaging with information enclosed in the correlation coefficient $\hat{w}_{12}$ in equation (4.5) to triple-intensity correlation imaging, we need to take into account all the coefficients $\hat{w}_{12}$, $\hat{w}_{13}$ and $\hat{w}_{23}$ in equation (4.6). Depending on the case in question the information about the object might be enclosed in just part of the coefficients while more generally it could be in all of them. We begin by calculating the visibility in the general case (case A) and then move to the specific case with one test arm (case B).

Case A: Generic setup With the generic setup from figure 4.2a, we assume that maximum information can be obtained from all the three correlation terms $\hat{w}_{12}$, $\hat{w}_{13}$ and $\hat{w}_{23}$, i.e., $0 \leq |\hat{w}_{\alpha\beta}| \leq 1$, $\alpha, \beta \in \{1,2,3\}$, $\alpha \neq \beta$, as implied by equation (4.3). Applying these extrema to equation (4.6) and inserting into the visibility definitions given by equations (4.9) and (4.11) we obtain [14, 15]

$$V_{\mathrm{C,A}}^{(3)} = \frac{3P^2+2}{3P^2+4}, \tag{4.13a}$$

$$V_{\mathrm{G,A}}^{(3)} = \frac{3P^2+2}{3P^2+3}, \tag{4.13b}$$

shown with the dashed lines in figures 4.4a and 4.5a, respectively.

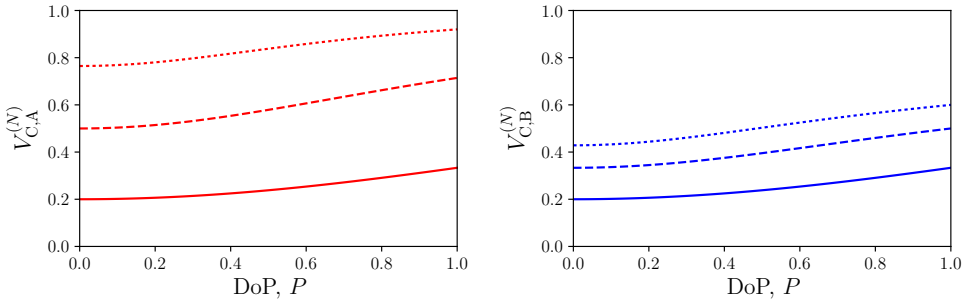

(a) Case A **(b)** Case B

Figure 4.4. Comparison of visibilities of the orders $N \in \{2,3,4\}$ according to Cao's definition, equation (4.9). The solid lines are for $N = 2$, the dashed lines are for $N = 3$ and the dotted lines are for $N = 4$.

Case B: Specific setup with one test arm In case B there is only one correlation coefficient in the normalised triple-intensity ICF given by equation (4.7). Again, by equation (4.3), the coefficient is limited between $0 \leq |\hat{w}_{13}| \leq 1$, and similarly to equation (4.13) we obtain the visibilities [15][3]

$$V_{\mathrm{C,B}}^{(3)} = \frac{5P^2+3}{7P^2+9} \tag{4.14a}$$

[3]There is a miscalculation in equation (30) in [15]. The correct visibility is given by equation (4.14b).

$$V_{\mathrm{G,B}}^{(3)} = \frac{5P^2+3}{6P^2+6}. \tag{4.14b}$$

These are illustrated in figures 4.4b and 4.5b with dashed lines.

4.2.3 Nth-order intensity correlation imaging

For Nth-order intensity correlation imaging we have N arms and $\triangle(N-1)$ correlation coefficients, as pointed out in section 4.1.3. Although there is no known analytical form of the normalised ICF, the necessary extrema of it have been calculated in section A.2 and those results can directly be used to calculate the visibility for any given order in cases A and B.

Case A: Generic setup Inserting equations (A.15) and (A.16) into the definitions given by equations (4.9) and (4.11), we obtain [11, 14]

$$V_{\mathrm{C,A}}^{(N)} = \frac{N!\left[(1+P)^{N+1}-(1-P)^{N+1}\right]-P\cdot 2^{N+1}}{N!\left[(1+P)^{N+1}-(1-P)^{N+1}\right]+P\cdot 2^{N+1}} \tag{4.15}$$

and [14]

$$V_{\mathrm{G,A}}^{(N)} = \frac{N!\left[(1+P)^{N+1}-(1-P)^{N+1}\right]-P\cdot 2^{N+1}}{N!\left[(1+P)^{N+1}-(1-P)^{N+1}\right]} \tag{4.16}$$

respectively. The visibilities for $N \in \{2,3,4\}$ are presented in figures 4.4a and 4.5a.

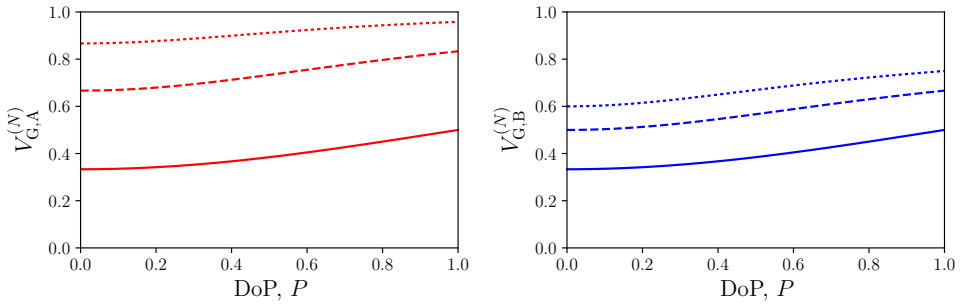

(a) Case A **(b)** Case B

Figure 4.5. Comparison of visibilities of the orders $N \in \{2,3,4\}$ according to Gatti's definition, equation (4.11). The solid lines are for $N = 2$, the dashed lines are for $N = 3$ and the dotted lines are for $N = 4$.

Case B Inserting equations (A.19) and (A.20) into the definitions given by equations (4.9) and (4.11), we obtain

$$V_{\mathrm{C,B}}^{(N)} = \frac{N\left[(1+P)^{N+1}-(1-P)^{N+1}\right]-2\left[(1+P)^{N}-(1-P)^{N}\right]}{N\left[(1+P)^{N+1}-(1-P)^{N+1}\right]+2\left[(1+P)^{N}-(1-P)^{N}\right]} \tag{4.17}$$

and

$$V_{\mathrm{G,B}}^{(N)} = \frac{N\left[(1+P)^{N+1} - (1-P)^{N+1}\right] - 2\left[(1+P)^{N} - (1-P)^{N}\right]}{N\left[(1+P)^{N+1} - (1-P)^{N+1}\right]} \tag{4.18}$$

respectively. These are presented in figures 4.4b and 4.5b for $N \in \{2,3,4\}$.

4.2.4 Conclusions on visibility

Focusing on the graphs in figures 4.4 and 4.5, we note that the visibility has an upwards trend for $N \in \{2,3,4\}$ when the DoP increases. We also note that the visibility grows considerably when the imaging order is increased. Using either definition for the visibility leads to the same physical conclusions, although they are normalised differently.

4.3 Signal-to-noise ratio

While the visibility is a measure of the contrast of the dark and bright areas of the image, there are also other factors affecting the image quality. A second important measure on the image quality is the assessment of the noisiness of the image. To perform classical ghost imaging we inherently need a noisy source; if there were no intensity fluctuations, we could not measure the intensity fluctuation correlation which contains the imaging information. In the following we calculate the noise pertaining to the source in the correlation imaging system without taking into account other sources of noise, such as those inherent to the beam splitter, the detector and other parts of the optical system.

We treat the fluctuating quantity $I_1 \cdots I_N$ as the signal. According to equation (2.10) the noise is given by the root-mean-square of the deviation from the mean signal [equation (2.9)], or

$$\mathrm{noise}(I_1 \cdots I_N) = \sqrt{\langle I_1^2 \cdots I_N^2 \rangle - \langle I_1 \cdots I_N \rangle^2}. \tag{4.19}$$

For Gaussian statistics, this quantity is always greater than zero. To compare the average signal to the noise associated with it, we define the signal-to-noise ratio (SNR) as [14, 15]

$$\mathrm{SNR}^{(N)} \equiv \frac{\langle I_1 \cdots I_N \rangle}{\mathrm{noise}(I_1 \cdots I_N)}. \tag{4.20}$$

Using the notation

$$\tilde{g}^{(2N)} \equiv \frac{\langle I_1^2 \cdots I_N^2 \rangle}{\langle I_1 \rangle^2 \cdots \langle I_N \rangle^2}, \tag{4.21}$$

equation (4.20) becomes

$$\mathrm{SNR}^{(N)} = \frac{g^{(N)}}{\sqrt{\tilde{g}^{(2N)} - \left[g^{(N)}\right]^2}}, \tag{4.22}$$

which can readily be used to calculate the SNR in various cases in the following subsections.

4.3.1 Double-intensity correlation imaging

Considering double-intensity correlation imaging, cases A and B introduced in section 4.1.1 have the same the SNR. The dark and bright areas of the image exhibit the SNRs [15]

$$\mathrm{SNR}\left[g^{(2)}_{\mathrm{min}}\right] = \frac{2}{\sqrt{P^4 + 6P^2 + 5}}, \tag{4.23a}$$

$$\mathrm{SNR}\left[g^{(2)}_{\mathrm{max}}\right] = \frac{P^2 + 3}{\sqrt{5P^4 + 54P^2 + 21}}, \tag{4.23b}$$

where we have used equations (4.22), (A.15), (A.16), (A.17), and (A.18) with $N = 2$ to calculate the results.

The behaviour of the SNR with respect to the DoP in the dark and bright areas of the image is shown with the solid lines in figures 4.6 and 4.7, respectively. In both areas the trend is for the SNR to decrease with the DoP. Also, the SNR is smaller in the bright areas when compared to the dark areas at a similar DoP. This is because the noise increases relatively more in the bright areas, although the signal also increases [15].

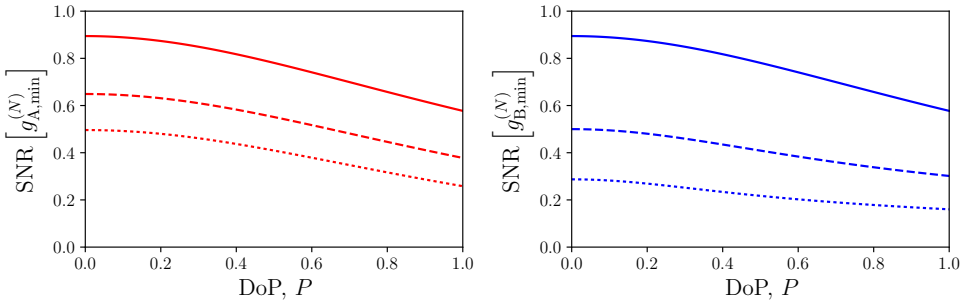

(a) Case A **(b)** Case B

Figure 4.6. Behaviour of the SNR in the dark areas of the image, $\mathrm{SNR}[g^{(N)}_{\Omega,\mathrm{min}}]$, for the orders $N \in \{2,3,4\}$ and $\Omega \in \{A,B\}$, as a function of the DoP. The solid lines are for $N = 2$, the dashed lines are for $N = 3$ and the dotted lines are for $N = 4$.

4.3.2 Third-order intensity correlations

While the visibility increased when moving to third-order intensity correlations, we will see that in triple-intensity imaging the quality of the image is worse when compared to double-intensity imaging when the SNR is used as the assessing quality parameter.

Case A Inserting $N = 3$ into equations (4.22), (A.15), (A.16), (A.17), and (A.18) we obtain

$$\mathrm{SNR}\left[g^{(3)}_{\mathrm{A,min}}\right] = \frac{2\sqrt{2}}{\sqrt{P^6 + 9P^4 + 27P^2 + 19}}, \tag{4.24}$$

$$\mathrm{SNR}\left[g^{(3)}_{\mathrm{max}}\right] = \frac{2\left(P^2 + 1\right)}{\sqrt{5P^6 + 101P^4 + 167P^2 + 31}}. \tag{4.25}$$

These are presented in with the dashed lines in figures 4.6a and 4.7. We note that at both extrema, the SNR decreases monotonically with the DoP. Additionally, the SNR is smaller when compared to second-order intensity correlations for any given DoP.

Case B In case B the SNR in the bright areas is the same as in case A. For the dark areas, similarly to equation (4.24), we obtain [now using equations (4.22), (A.19), and (A.21)]

$$\mathrm{SNR}\left[g^{(3)}_{\mathrm{B,min}}\right] = \sqrt{\frac{P^2 + 3}{3P^4 + 29P^2 + 12}}. \tag{4.26}$$

Equation (4.26) is shown with the dashed line in figure 4.6b. When comparing cases A and B presented in figures 4.6a and 4.6b, respectively, case B exhibits smaller SNR at any DoP, although the decrease is not as large as the difference to the SNR of double-intensity imaging. One reason for the smaller SNR in case B is that, although the correlation image is brighter in case B, it has more noise. That is, although the fact that $g^{(3)}_{\mathrm{B,min}} > g^{(3)}_{\mathrm{A,min}}$is a positive thing for the SNR, the noisiness is dominated by the fact that $\tilde{g}^{(6)}_{\mathrm{B,min}} > \tilde{g}^{(6)}_{\mathrm{A,min}}$ and this negates the positive affects.

4.3.3 Nth-order intensity correlations

Now, in general, from equation (4.22), the SNR extrema are

$$\mathrm{SNR}\left[g^{(N)}_{\Omega,\mathrm{ext}}\right] = \left\{\mathrm{fr}^{(N)}_{\Omega,\mathrm{ext}} - 1\right\}^{-1/2}, \tag{4.27}$$

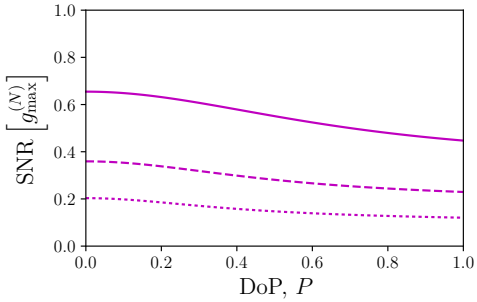

Figure 4.7. The SNR in the bright areas of the image, SNR$[g^{(N)}_{\max}]$, is the same for cases A and B. Here the results are presented for the orders $N \in \{2,3,4\}$, with the solid lines drawn for $N = 2$, the dashed lines for $N = 3$ and the dotted lines for $N = 4$.

where

$$\mathrm{fr}^{(N)}_{\Omega,\mathrm{ext}} \equiv \frac{\tilde{g}^{(2N)}_{\Omega,\mathrm{ext}}}{\left[g^{(N)}_{\Omega,\mathrm{ext}}\right]^2}, \tag{4.28}$$

$\Omega \in \{A, B\}$, ext $\in \{\min, \max\}$. Using equations (A.15) to (A.22) we obtain

$$\mathrm{fr}^{(N)}_{\mathrm{A,min}} = \frac{\tilde{g}^{(2N)}_{\mathrm{A,min}}}{\left[g^{(N)}_{\mathrm{A,min}}\right]^2} = \left(\frac{P^2+3}{2}\right)^N, \tag{4.29}$$

$$\mathrm{fr}^{(N)}_{\mathrm{A,max}} = 2P\binom{2N}{N}\frac{\left[(1+P)^{2N+1} - (1-P)^{2N+1}\right]}{\left[(1+P)^{N+1} - (1-P)^{N+1}\right]^2}, \tag{4.30}$$

$$\mathrm{fr}^{(N)}_{\mathrm{B,min}} = P(P^2+3)\binom{2N-2}{N-1}\cdot\frac{\left[(1+P)^{2N-1} - (1-P)^{2N-1}\right]}{\left[(1+P)^{N} - (1-P)^{N}\right]^2}, \tag{4.31}$$

$$\mathrm{fr}^{(N)}_{\mathrm{B,max}} = 2P\binom{2N}{N}\frac{\left[(1+P)^{2N+1} - (1-P)^{2N+1}\right]}{\left[(1+P)^{N+1} - (1-P)^{N+1}\right]^2}. \tag{4.32}$$

Using these gives us the SNR extrema in both cases A and B for any order and DoP. These have been used to draw the SNR for $N \in \{2,3,4\}$ in figures 4.6 and 4.7. Analysis of these results follows.

Case A Referring to figure 4.6a and figure 4.7, we see that the SNR becomes smaller as the DoP increases for all the orders $N \in \{2,3,4\}$. This is due to the fact that, although the signal becomes larger with increasing DoP, the noise grows proportionally faster. The same is true for the increasing imaging order; moving to a larger imaging order gives a better signal, but the noise is increased proportionally more, bringing the SNR down with the imaging order, as can be seen when moving from the solid lines ($N = 2$) to the dashed lines ($N = 3$) or from the dashed lines to the dotted lines ($N = 4$).

Comparing the SNR in the dark and bright areas of the image for a similar order, we note that the SNR is lower in the bright areas of the image when compared to the dark areas. The reason for this is that, again, although the signal is higher, the increased noise brings the SNR down for the bright areas.

Case B In case B, the same trend can be seen in figure 4.6b and figure 4.7, for the behaviour of the SNR with respect to the DoP, imaging order and brightness of the image.

When compared to case A, case B exhibits lower SNR in the dark areas of the image for the orders $N \in \{3,4\}$. This is due to the larger background in case B, contributing to an increased noise. The SNR in the bright areas of the image is the same for both cases.

4.4 Contrast-to-noise ratio

The visibility and SNR give valuable information on the image quality of ghost imaging, each from very different characteristics of the resulting image. A third, and possibly the most useful of the image quality parameters, is the contrast-to-noise ratio (CNR), which has been researched in several publications [15,33,35,36,39,40].

While using the CNR, both the contrast and the noise in the image are taken into account for a more balanced assessment of the image quality. The previous analysis in this chapter on the visibility and SNR in various cases will help us in understanding the reasons why the CNR behaves as it does in similar cases in this section.

The CNR is defined as [15,35,39]

$$\mathrm{CNR}\left[g^{(N)}\right] \equiv \frac{\langle I_1 \cdots I_N \rangle_{\max} - \langle I_1 \cdots I_N \rangle_{\min}}{\sqrt{\frac{1}{2}\left[\mathrm{noise}^2_{\max}(I_1 \cdots I_N) + \mathrm{noise}^2_{\min}(I_1 \cdots I_N)\right]}}. \tag{4.33}$$

Similar definitions are used in [33,36,40], differing mainly in normalisation. Using equations (4.19) and (4.21) the CNR can be expressed in the form

$$\mathrm{CNR}\left[g^{(N)}\right] = \frac{g^{(N)}_{\max} - g^{(N)}_{\min}}{\sqrt{\frac{1}{2}\left[\tilde{g}^{(2N)}_{\max} - \left[g^{(N)}_{\max}\right]^2 + \tilde{g}^{(2N)}_{\min} - \left[g^{(N)}_{\min}\right]^2\right]}}. \tag{4.34}$$

4.4.1 Double-intensity correlation imaging

Inserting equations (A.15), (A.16), (A.17), and (A.18) with $N = 2$ into equation (4.34) we obtain the CNR for double-intensity correlation imaging [15]

$$\mathrm{CNR}\left[g^{(2)}\right] = \frac{P^2 + 1}{\sqrt{3P^4 + 30P^2 + 13}}. \tag{4.35}$$

From the solid lines in figure 4.8 it is seen that the CNR does not change significantly as a function of the DoP. From the analysis on the visibility in

section 4.2 we know that the contrast is improved as the DoP becomes larger and from the analysis on the SNR in section 4.3 we know that the noise increases with the DoP. Thus, we can infer that the CNR holds approximately constant because the tendencies in the visibility and noise mostly cancel each other out. However, the CNR does change slightly with the DoP, with the highest CNR achieved for fully polarised light for a value equal to $\sqrt{2/23} \approx 0.29$ [15].

4.4.2 Third-order intensity correlations

Case A Using equations (4.34), (A.15), (A.16), (A.17), and (A.18) with $N = 3$ we obtain [15]

$$\mathrm{CNR}\left[g_{\mathrm{A}}^{(3)}\right] = \frac{12P^2 + 8}{\sqrt{91P^6 + 1827P^4 + 3033P^2 + 577}}. \tag{4.36}$$

As shown in figure 4.8a with the dashed line, the CNR decreases monotonically with the increase of the DoP. This is contrary to double-intensity imaging. However, the decrease is not significant and the CNR stays in the range $0.27 \lesssim \mathrm{CNR}[g_{\mathrm{A}}^{(3)}] \lesssim 0.33$. Although the CNR is smaller for fully polarised light when compared to second-order ghost imaging, fully unpolarised light achieves better CNR when compared to double-intensity imaging.

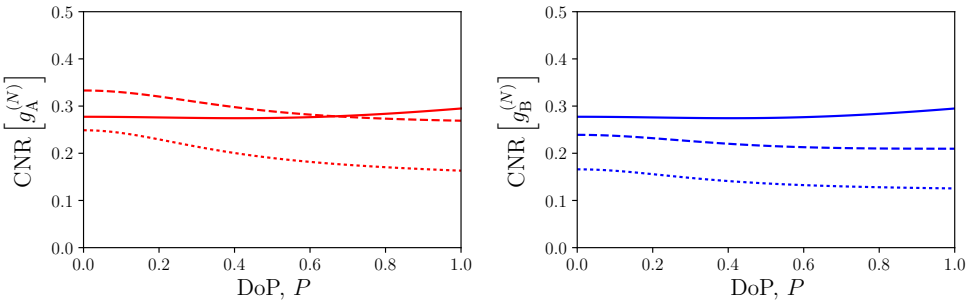

(a) Case A **(b)** Case B

Figure 4.8. Comparison of the CNR of the image for the orders $N \in \{2, 3, 4\}$. The solid lines are for $N = 2$, the dashed lines are for $N = 3$ and the dotted lines are for $N = 4$.

Case B Using equations (4.34), (A.19), (A.20), (A.21), and (A.22) with $N = 3$ we obtain [15]

$$\mathrm{CNR}\left[g_{\mathrm{B}}^{(3)}\right] = \frac{\sqrt{2}\left(5P^2 + 3\right)}{\sqrt{48P^6 + 947P^4 + 1602P^2 + 315}}. \tag{4.37}$$

As in case A, the CNR in case B decreases monotonically with the DoP, as shown with the dashed line in figure 4.8b. In case B the CNR stays in the

range $0.21 \lesssim \mathrm{CNR}[g_{\mathrm{B}}^{(3)}] \lesssim 0.24$ and is thus smaller than the CNR of both the third-order case A and the double-intensity imaging setups at any DoP.

4.4.3 Nth-order intensity correlations

Case A Using equations (4.34), (A.15), (A.16), (A.17), and (A.18) we obtain

$$\mathrm{CNR}\left[g_{\mathrm{A}}^{(N)}\right] = \frac{N! \cdot h_{(N+1)} - P \cdot 2^{N+1}}{\sqrt{P(2N)! \cdot h_{(2N+1)} + P^2 2^{N+1}(P^2+3)^N - \frac{1}{2}\left(N!\right)^2 h_{(N+1)}^2 - P^2 2^{2N+1}}}, \tag{4.38}$$

where

$$h_{(n)} \equiv (1+P)^n - (1-P)^n.$$

This result is presented for $N \in \{2,3,4\}$ in figure 4.8a.

As discussed in section 4.4.1, the CNR is almost constant as a function of the DoP in double-intensity correlation imaging, with the maximum CNR achieved with fully polarised light. However, for the higher orders shown in figure 4.8a the CNR decreases monotonically with the increase of the DoP, although the decrease is not as significant as with the SNR.

Judging by the CNR, using unpolarised light is beneficial with third- and fourth-order intensity correlations. The highest CNR is given by third-order imaging with unpolarised light; when using polarised light double-intensity imaging produces the best CNR. The differences between second- and third-order intensity correlations are not significant, but fourth-order correlations are noticeably behind the lower-order correlations in terms of the CNR, especially with fully polarised light.

From the analysis related to the other quality parameters, it is evident that the mixed results related to the CNR are an indication of the features of the visibility and SNR battling; while the visibility increases with the growing DoP and imaging order, the SNR behaves oppositely.

Case B Using equations (4.34), (A.19), (A.20), (A.21), and (A.22) we obtain

$$\mathrm{CNR}\left[g_{\mathrm{B}}^{(N)}\right] = \frac{N! \cdot h_{(N+1)} - 2(N-1)! \cdot h_{(N)}}{\sqrt{P(2N)! h_{(2N+1)} + 2P(P^2+3)(2N-2)! h_{(2N-1)} - \frac{1}{2}\left(N!\right)^2 h_{(N+1)}^2 - 2\left[(N-1)!\right]^2 h_{(N)}^2}}. \tag{4.39}$$

Mostly the same conclusions, as made for case A, can be made from figure 4.8b for case B. The second-order setup is the same as in case A. The third- and fourth-order intensity correlations exhibit a similar downwards trend with the increase of the DoP. The difference is that in case B the CNR is smaller for higher order imaging when compared to case A. In case B, the best CNR is achieved with fully polarised light in a double-intensity imaging arrangement.

4.5 Resolution

Since the resolution is not affected by changing the DoP of the source, the subject of the ghost image resolution is not studied in a quantitative manner here. However, a brief qualitative analysis is provided.

Comparing the ghost imaging results in equations (3.20) and (3.22) (which are obtained using a completely incoherent source and a Gaussian-Schell model source, respectively), the first has an infinite resolution reproduction of the object transmission function in the form $|T(\mathbf{r}_1)|^2$ and the second has blurred reproduction of the object transmission function in the form

$$\left| \int_{-\infty}^{\infty} \mathrm{d}^2 r \exp\left[\frac{ik}{2d}\mathbf{r}^2 - \frac{(\mathbf{r}_1 - \mathbf{r})^2}{2\sigma_g^2} \right] T(\mathbf{r}) \right|^2 . \tag{4.40}$$

We note that the second form is practically the convolution of the object transfer function in the first form [multiplied by $\exp\left(ik\mathbf{r}_1^2/2d\right)$] and the Gaussian $\exp\left[-(\mathbf{r}_1-\mathbf{r})^2/2\sigma_g^2\right]$. Both $|T(\mathbf{r}_1)|^2$ and equation (4.40) behave similarly when the changes in $T(\mathbf{r})$ are at a large scale compared to the transverse coherence width, σ_g [7]. Thus, the smaller the coherence width, the more accurately $T(\mathbf{r})$ is obtained and the larger the resolution of the imaging [7]. When taking the concept of the effective source into account, an additional note can be made that the smaller the coherence width of the *effective source*, the larger the resolution of the imaging.

In higher-order imaging, the spreading effect of the coherence width will become less apparent as the coherence function is raised to higher powers in more and more terms of the measured ICF. When the resolution is defined as the half-width of when the ICF drops to a proportion of its maximum, it will decline to this point faster with higher orders, resulting in a higher resolution as the order of imaging increases (the coherence width effectively decreases with the imaging order [8]). A more complete analysis of this higher order imaging resolution with experimental results is presented by Cao *et al.* [8].

5. Conclusions

The fictitious plane of the effective source (FPES) has previously been shown to be convenient for simplifying the calculations related to (electromagnetic) ghost imaging and ghost diffraction. It was shown that not only does a completely incoherent source retain its form at the FPES, but so does a Gaussian-Schell model source when assuming a sufficiently wide source. Using the FPES and the retained forms of the sources can greatly ease the analysis of various ghost imaging setups.

Analytical forms for the ghost imaging intensity correlation functions (ICFs) needed to calculate the image quality for any order of imaging were presented for two different cases. Case A was a general, "optimal" situation where the image quality reached its maximum for the imaging order in question, and case B was based on a realistic case with one test arm and multiple reference arms. In addition to the analytical forms of the ICFs, a computational method was described, and it can be used to calculate the image quality for arbitrary order intensity correlations with vectorial light.

Taking into consideration all of these results together, a very robust and powerful way of analysing various order ghost imaging setups with an electromagnetic source and polarising elements in the system has been provided.

Another big part of this work was the image quality analysis. Using the FPES and the analytical results for the higher-order correlations together with a generalisation of the Schwarz inequality, image quality analysis was performed based mainly on three different quality parameters.

As noted in earlier work for case A, it was seen that the *visibility* improves when the degree of polarisation (DoP) and imaging order increase. In this work it was shown that the same is true for case B, while the visibility is smaller at any given order in case B when compared to case A at that same order.

The *signal-to-noise ratio* (SNR) was studied separately for the bright and dark

areas of the image. In both areas the SNR behaved quite oppositely to the visibility when the DoP or imaging order were increased, with the double-intensity cases with fully unpolarised light achieving the best SNR and the higher-order imaging cases having worse SNR, especially with fully polarised light. For the dark areas in third- and higher-order setups the SNR was larger in case A when compared to case B, while the bright areas exhibited a similar SNR in both cases.

The results based on the *contrast-to-noise ratio* (CNR) were mixed. For second-order imaging the CNR was almost constant and achieved its maximum with fully polarised light. All the higher-order cases studied featured a decrease in the CNR with an increase in the DoP. In case A, the highest CNR was achieved in third-order imaging with fully unpolarised light, but the CNR was larger in the double-intensity setup than the triple-intensity setup when limiting the analysis to fully polarised light. Moving to the fourth-order setup the CNR became smaller, independent of the DoP. In the higher-order setups related to case B, the CNR always became smaller when increasing the imaging order.

In addition to the three main parameters studied here, also *resolution* was discussed, but since it was not directly affected by a change in the DoP, and since the effect of the imaging order on the resolution has been studied elsewhere, no in-depth analysis was reproduced here. Nevertheless, it was noted that increasing the imaging order can increase the resolution slightly, while decreasing the transverse coherence width of the source (or the effective source) increases the resolution noticeably. Using the concept of the effective source and the calculated behaviour of the Gaussian-Schell model source at the FPES, resolution analysis of ghost imaging setups is less complicated.

To sum up, we have presented both powerful analytical methods and robust computational methods for the analysis of complex electromagnetic correlation imaging setups. Our results on visibility and SNR give good insight on the behaviour of the setups we chose to analyse when trying to achieve better contrast or reduce noise. The CNR takes both the contrast and the noise into account, and our results might help in choosing the direction taken to improve the image quality of a certain ghost imaging setup. The concept of the FPES is a powerful tool that can be further developed for different kinds of setups to ease their analysis, and to e.g. assess their resolution effectively. All combined, the results presented here are especially important for the analysis of electromagnetic ghost imaging setups and applications such as ghost polarimetry, where the electromagnetic nature of light needs to be taken into account.

A. Analysing higher-order intensity correlations

To evaluate the image quality of higher-order ghost imaging setups we need to calculate higher-order intensity correlations. For assessing an arbitrary order intensity correlation, there are two main approaches that we can take. In the first approach we examine a very general case while taking into account the electromagnetic nature of light. With certain assumptions, we are able to obtain the extrema of the intensity correlations.In the second approach we introduce computational methods which can be used to examine values in between the extrema.

Analytical method	Method with algorithms
Analytical form applicable to all orders.	The computational time and memory available limit the order that can be studied as both grow faster than $N!$
We assume that $\mathbf{W}_{\alpha\beta} = \mathbf{J}_0 \hat{W}_{\alpha\beta}$ holds.	
We assume that $\mathbf{J}_0$ is diagonalisable with a unitary transformation.	
Only applies to cases A and B, although it could be generalised to other cases as well	Applies to various cases; our implementation assumes there is no phase difference between the arms
Can only be used for the extrema of the relevant ICFs.	Applies to any value of the ICFs; the correlation parameters are fully adjustable (although real in the python implementation).

Table A.1. The limitations and strengths of the analytical method introduced in section A.2 and the method using algorithms in section A.3.

A comparison of the limitations and strengths of the two methods is presented in table A.1. In section A.2 we introduce the analytical method to obtain the analytical forms for Nth-order correlations in the ghost imaging cases A

and B introduced in section 4.1. The computational method for calculating an arbitrary order normalised ICF is introduced in section A.3.

A.1 Common mathematical results

The results presented here are used to aid the calculations in the main text and later sections in this chapter.

A.1.1 Schwarz inequality generalisation

This result is used to simplify the calculations when using the effective source which is located at a fictitious plane away from the actual source. The proof has been adapted from the tip for the alternative derivation for the Schwarz inequality provided in [19].

Theorem A.1. *The inequality*

$$\left| \iint_{-\infty}^{\infty} \mathrm{d}x\mathrm{d}y f^*(x)\mu(x-y)g(y) \right|^2$$
$$\leq \iint_{-\infty}^{\infty} \mathrm{d}x\mathrm{d}x' f^*(x)\mu(x-x')f(x') \iint_{-\infty}^{\infty} \mathrm{d}y\mathrm{d}y' g^*(y)\mu(y-y')g(y'), \tag{A.1}$$

where $\mu(x) = \mu(-x)$ *and* $\mu(x) \geq 0$, $\forall x \in \mathbb{R}$, *holds for any functions* $f, g \in \mathbb{C}$.

Proof. Let us define the complex function $\psi(x,y) = f(x)g(y) - g(x)f(y)$, $\psi, f, g \in \mathbb{C}$. Since the integrand is always nonnegative it holds that

$$0 \leq \iiiint_{-\infty}^{\infty} \mathrm{d}x\mathrm{d}x'\mathrm{d}y\mathrm{d}y'\mu(x-x')\mu(y-y') \left|\psi(x,y)\right|^2, \tag{A.2}$$

for any nonnegative real function μ for which $\mu(x) = \mu(-x)$. Now let us define two helper functions

$$F(x) = \int_{\infty}^{\infty} \mathrm{d}x'\mu(x-x')f(x'),$$
$$G(y) = \int_{\infty}^{\infty} \mathrm{d}y'\mu(y-y')g(y').$$

Using these, equation (A.2) can be written in the form

$$0 \leq \iint_{-\infty}^{\infty} \mathrm{d}x\mathrm{d}y \left[f^*(x)G^*(y) - g^*(x)F^*(y)\right]\left[F(x)g(y) - G(x)f(y)\right]$$
$$= \iint_{-\infty}^{\infty} \mathrm{d}x\mathrm{d}y f^*(x)F(x)G^*(y)g(y) + \iint_{-\infty}^{\infty} \mathrm{d}x\mathrm{d}y g^*(x)G(x)F^*(y)f(y)$$

$$-\iint_{-\infty}^{\infty} \mathrm{d}x\mathrm{d}y g^*(x)F(x)F^*(y)g(y) - \iint_{-\infty}^{\infty} \mathrm{d}x\mathrm{d}y f^*(x)G(x)G^*(y)f(y). \quad \text{(A.3)}$$

A change of variables and using the fact that $f^*(x)F(x) = F^*(x)f(x)$ and $g^*(x)F(x) = G^*(x)f(x)$ enables us to write

$$\iint_{-\infty}^{\infty} \mathrm{d}x\mathrm{d}y g^*(x)F(x)F^*(y)g(y) \leq \iint_{-\infty}^{\infty} \mathrm{d}x\mathrm{d}y f^*(x)F(x)G^*(y)g(y). \quad \text{(A.4)}$$

Again, using the definitions for F, G and with a change of variables for the integrations we arrive at equation (A.1). □

A.1.2 Matrix traces

Both the analytical and the computational method to calculate the image quality rely on the following theorem.

Theorem A.2. *The property*

$$\sum_{i_1,\ldots,i_n \in \{x,y\}} A_{1,i_1 i_2} A_{2,i_2 i_3} \cdots A_{n,i_n i_1} = \mathrm{tr}\left(\mathbf{A}_1 \cdots \mathbf{A}_n\right), \quad \text{(A.5)}$$

$n \in \mathbb{N}$ *, holds for any arbitrary matrices*

$$\mathbf{A}_\alpha = \begin{pmatrix} A_{\alpha,xx} & A_{\alpha,xy} \\ A_{\alpha,yx} & A_{\alpha,yy} \end{pmatrix}, \quad \text{(A.6)}$$

$\alpha \in \{1, \ldots, n\}$.

Proof. We use mathematical induction:

1. Basis: Equation (A.5) holds for $n = 1$:

$$\sum_{i_1 \in \{x,y\}} A_{1,i_1 i_1} = \mathrm{tr}\left(\mathbf{A}_1\right). \quad \text{(A.7)}$$

2. Inductive step: We make the assumption that equation (A.5) holds for $n = k$. Next we study the case of $n = k + 1$:

$$\sum_{i_1,\ldots,i_{k+1} \in \{x,y\}} A_{1,i_1 i_2} \cdots A_{k-1,i_{k-1} i_k} A_{k,i_k i_{k+1}} A_{k+1,i_{k+1} i_1} \quad \text{(A.8a)}$$

$$= \sum_{i_1,\ldots,i_k \in \{x,y\}} A_{1,i_1 i_2} \cdots A_{k-1,i_{k-1} i_k} B_{k,i_k i_1} \quad \text{(A.8b)}$$

$$= \mathrm{tr}\left(\mathbf{A}_1 \cdots \mathbf{A}_{k-1} \mathbf{B}_k\right) \quad \text{(A.8c)}$$

$$= \mathrm{tr}\left(\mathbf{A}_1 \cdots \mathbf{A}_{k-1} \mathbf{A}_k \mathbf{A}_{k+1}\right), \quad \text{(A.8d)}$$

where $\mathbf{B}_k \equiv \mathbf{A}_k \mathbf{A}_{k+1}$. Equation (A.8b) follows from the definition of $\mathbf{B}_k$ with its elements satisfying $B_{k,i_k i_1} = \sum_{i_{k+1} \in \{x,y\}} A_{k,i_k i_{k+1}} A_{k+1,i_{k+1} i_1}$, $i_k, i_1 \in \{x, y\}$, and

equation (A.8c) follows from the assumption that equation (A.5) holds for $n = k$.

Since equation (A.5) holds for both the basis and the inductive step, it holds for $n \in \mathbb{N}$ due to the principle of mathematical induction. □

A.2 Analytical forms for some Nth-order correlations

Referring to section 4.1, let us examine the Nth-order ghost imaging which has no polarisation state altering components in any of the arms of the setup and the polarisation state of the source is described by the polarisation matrix $\mathbf{J}_0$.

We choose the xy-coordinate system in such a manner that the source's polarisation matrix is diagonal[1] as in equation (2.20), that is, $\mathbf{J}_0 = \mathrm{diag}(J_1, J_2)$. This results in the x- and y-components of the field being completely uncorrelated, i.e., $\langle I_{x,\alpha} I_{y,\beta} \rangle = \langle I_{x,\alpha} \rangle \langle I_{y,\beta} \rangle$ for all $\alpha, \beta \in \{1, \dots N\}$.

In general, the Nth-order intensity correlation function (ICF), separated into the different components of the intensities, is given by equation (2.26). Due to the uncorrelation in the chosen basis we can rearrange the x- and y-intensities into their own ensemble average, with the ICF becoming [11]

$$G^{(N)}(\mathbf{r}_1, \dots, \mathbf{r}_N) = \sum_{m=0}^{N} \sum_{\binom{N}{m}} \left\langle \prod_{\alpha \in S_x} I_{x,\alpha} \right\rangle \left\langle \prod_{\beta \in S_y} I_{y,\beta} \right\rangle, \tag{A.9}$$

where the sum denoted by the binomial $\binom{N}{m}$ stands for the sum over all possible arrangements in which m intensities can be arranged out of the total number of N intensities. The products (denoted by $\prod$) inside the ensemble averages are over the sets $S_x = \{\alpha_1, \dots, \alpha_m\}$ and $S_y = \{\beta_1, \dots, \beta_{N-m}\}$, where the union and intersection obey $S_x \cup S_y = \{1, \dots, N\}$ and $S_x \cap S_y = \emptyset$ with all arrangements.

Using the Gaussian moment theorem [see equation (2.27)] twice for the disconnected intensity correlations, equation (A.9) becomes

$$\begin{aligned} G^{(N)}(\mathbf{r}_1, \dots, \mathbf{r}_N) = \sum_{m=0}^{N} \sum_{\binom{N}{m}} & \left[\sum_{m!} \left\langle E^*_{x,\alpha_1} \underline{E_{x,\alpha_1}} \right\rangle \cdots \left\langle E^*_{x,\alpha_m} \underline{E_{x,\alpha_m}} \right\rangle \right] \\ & \times \left[\sum_{(N-m)!} \left\langle E^*_{y,\beta_1} \underline{E_{y,\beta_1}} \right\rangle \cdots \left\langle E^*_{y,\beta_{N-m}} \underline{E_{y,\beta_{N-m}}} \right\rangle \right] \end{aligned} \tag{A.10}$$

[1] As seen in section 2.3.3, the polarisation matrix of the source is always diagonalisable with a unitary transformation. Since a unitary transformation does not change the observables, namely the trace, no loss of generality is incurred by assuming that $\mathbf{J}_0$ is diagonal.

where summations in the square parenthesis are performed while permuting the underlined terms in $m!$ and $(N-m)!$ different ways.

From equation (4.1) we may infer that

$$\left\langle E^*_{x,\alpha} E_{x,\beta} \right\rangle = J_1 \hat{W}_{\alpha\beta},$$
$$\left\langle E^*_{y,\alpha} E_{y,\beta} \right\rangle = J_2 \hat{W}_{\alpha\beta},$$

and from the definition of the DoP from equation (2.21) we obtain

$$\frac{J_2}{J_1} = \frac{1-P}{1+P}.$$

Using these we arrive at

$$G^{(N)}(\mathbf{r}_1,\ldots,\mathbf{r}_N) = J_1^N \sum_{m=0}^{N} \sum_{\binom{N}{m}} \left[\sum_{m!} \hat{W}_{\alpha_1\underline{\alpha_1}} \cdots \hat{W}_{\alpha_m\underline{\alpha_m}} \right] \times \left[\left(\frac{1-P}{1+P} \right)^{N-m} \sum_{(N-m)!} \hat{W}_{\beta_1\underline{\beta_1}} \cdots \hat{W}_{\beta_{N-m}\underline{\beta_{N-m}}} \right]. \quad \text{(A.11)}$$

To normalise this we take advantage of the result

$$\prod_{\alpha=1}^{N} \langle I_\alpha \rangle = \left(\frac{2}{1+P} \right)^N J_1^N \prod_{\alpha=1}^{N} \hat{W}_{\alpha\alpha}, \quad \text{(A.12)}$$

where we used $\langle I_i \rangle = \operatorname{tr} \mathbf{W}_{ii} = \operatorname{tr} \mathbf{J}_0 \hat{W}_{ii}$ and $\operatorname{tr} \mathbf{J}_0 = J_1 + J_2 = 2J_1/(1+P)$. Inserting equations (A.11) and (A.12) into the definition of the normalised ICF [equation (2.25)] we obtain

$$g^{(N)}(\mathbf{r}_1,\ldots,\mathbf{r}_N) = \left(\frac{1+P}{2} \right)^N \sum_{m=0}^{N} \sum_{\binom{N}{m}} \left[\sum_{m!} \hat{w}_{\alpha_1\underline{\alpha_1}} \cdots \hat{w}_{\alpha_m\underline{\alpha_m}} \right] \times \left[\left(\frac{1-P}{1+P} \right)^{N-m} \sum_{(N-m)!} \hat{w}_{\beta_1\underline{\beta_1}} \cdots \hat{w}_{\beta_{N-m}\underline{\beta_{N-m}}} \right], \quad \text{(A.13)}$$

where $\hat{w}_{\alpha\beta}$ is the normalised correlation parameter defined in equation (4.4). This is as far as we get without knowing the values of of the correlation parameters. Next we consider cases A and B as introduced in section 4.1.

Case A: Generic setup In the generic case (figure 4.3a), the minimum of equation (A.13) is achieved when $\hat{w}_{\alpha\beta} = 0$ for all $\alpha \neq \beta$. In this case only one term survives from the summations over the $m!$ and $(N-m)!$ permutations. All the terms in the sum over $\binom{N}{m}$ combinations are the same. We have

$$g^{(N)}_{\mathrm{A,min}}(\mathbf{r}_1,\ldots,\mathbf{r}_N) = 1, \quad \text{(A.14)}$$

since $\hat{w}_{\alpha\alpha} = 1$ for all $\alpha \in \{1,\ldots,N\}$ (follows directly from the definition of $\hat{w}_{\alpha\beta}$) and

$$\sum_{m=0}^{N} \binom{N}{m} \left(\frac{1-P}{1+P} \right)^{N-m} = \left(\frac{2}{1+P} \right)^N$$

due to the Newton binomial theorem. The same result can be achieved by using the fact that none of the intensities are correlated at the minimum, i.e., $\langle I_\alpha I_\beta \rangle_{\min} = \langle I_\alpha \rangle \langle I_\beta \rangle$ for all $\alpha \neq \beta$. With this reasoning we have

$$g^{(N)}_{\mathrm{A,min}}(\mathbf{r}_1, \ldots, \mathbf{r}_N) = \frac{\prod_{\alpha=1}^{N} \langle I_\alpha \rangle}{\prod_{\alpha=1}^{N} \langle I_\alpha \rangle} = 1. \tag{A.15}$$

We will return to this way of using the uncorrelation of the intensities at the minimum in other cases.

The maximum of equation (A.11) is achieved when $|\hat{w}_{\alpha\beta}| = 1 \forall \alpha, \beta \in \{1, \ldots, N\}$ and there is no phase difference when multiplying over the groups $S_k \forall \kappa \in \{x, y\}$. This follows from the generalised Schwarz inequality given by equation (4.3). Thus, for an ideal maximum, the normalised correlation parameter satisfies the system of equations

$$\begin{aligned} \hat{w}_{\alpha\beta} &= e^{i\phi_{\alpha\beta}}, \\ \sum_{\alpha \in S_\kappa} \phi_{\alpha\underline{\alpha}} &= 2\pi n, \end{aligned}$$

where the underlined indices are permuted while summing over all possible permutations of α within S_k and $n \in \mathbb{Z}$. In this case all the terms in the summation over the $m!$ and $(N-m)!$ permutations, and the terms in the summation over $\binom{N}{m}$ combinations are the same and equal to unity. Equation (A.11) becomes

$$g^{(N)}_{\mathrm{A,max}}(\mathbf{r}_1, \ldots, \mathbf{r}_N) = \frac{N!}{P \cdot 2^{N+1}} \left[(1+P)^{N+1} - (1-P)^{N+1} \right], \tag{A.16}$$

since

$$\begin{aligned} \sum_{m!} \hat{w}_{\alpha_1\underline{\alpha_1}} \cdots \hat{w}_{\alpha_m\underline{\alpha_m}} &= m!, \\ \sum_{(N-m)!} \hat{w}_{\beta_1\underline{\beta_1}} \cdots \hat{w}_{\beta_{N-m}\underline{\beta_{N-m}}} &= (N-m)!, \\ \sum_{\binom{N}{m}} m!(N-m)! &= N!, \\ \sum_{m=0}^{N} \left(\frac{1-P}{1+P} \right)^{N-m} &= \frac{1+P}{2P} \left[1 - \left(\frac{1-P}{1+P} \right)^{N+1} \right]. \end{aligned}$$

To calculate the noise related to the system we introduced the normalised version of

$$\tilde{G}^{(2N)}(\mathbf{r}_1, \ldots, \mathbf{r}_N) \equiv \left\langle I_1^2 \cdots I_N^2 \right\rangle$$

in equation (4.21). The minimum of $\tilde{G}^{(2N)}$ has no other correlations besides the unavoidable self-correlations of the squared intensities, that is,

$$\left\langle I_1^2 \cdots I_N^2 \right\rangle_{\min} = \left\langle I_1^2 \right\rangle \cdots \left\langle I_N^2 \right\rangle.$$

Using this logic, the minimum of $\tilde{g}_{\mathrm{A}}^{(2N)}$ is

$$\tilde{g}_{\mathrm{A,min}}^{(2N)}(\mathbf{r}_1,\ldots,\mathbf{r}_N) = \left[g_{\mathrm{A,max}}^{(2)}\right]^N = \left(\frac{P^2+3}{2}\right)^N. \tag{A.17}$$

For the maximum we note that the self correlations are equal to the maximum correlation and thus

$$\begin{aligned}\tilde{g}_{\mathrm{A,max}}^{(2N)}(\mathbf{r}_1,\ldots,\mathbf{r}_N) &= g_{\mathrm{A,max}}^{(2N)} \\ &= \frac{(2N)!}{P\cdot 2^{2N+1}}\left[(1+P)^{2N+1}-(1-P)^{2N+1}\right].\end{aligned} \tag{A.18}$$

Case B In the specific case introduced in figure 4.3b there are $N-1$ identical reference arms yielding an ever-present maximal correlation between them. The minimum correlation is thus equal to the maximum correlation between $N-1$ arms. The maximum correlation is the same as in case A. The normalised extrema are

$$\begin{aligned}g_{\mathrm{B,min}}^{(N)}(\mathbf{r}_1,\ldots,\mathbf{r}_N) &= g_{\mathrm{A,max}}^{(N-1)}(\mathbf{r}_1,\ldots,\mathbf{r}_{N-1}) \\ &= \frac{(N-1)!}{P\cdot 2^N}\left[(1+P)^N-(1-P)^N\right],\end{aligned} \tag{A.19}$$

$$\begin{aligned}g_{\mathrm{B,max}}^{(N)}(\mathbf{r}_1,\ldots,\mathbf{r}_N) &= g_{\mathrm{A,max}}^{(N)}(\mathbf{r}_1,\ldots,\mathbf{r}_N) \\ &= \frac{N!}{P\cdot 2^{N+1}}\left[(1+P)^{N+1}-(1-P)^{N+1}\right].\end{aligned} \tag{A.20}$$

Similarly $\tilde{G}_{\mathrm{B,min}}^{(2N)}(\mathbf{r}_1,\ldots,\mathbf{r}_N) = \langle I_1^2\cdots I_{N-1}^2\rangle\langle I_N^2\rangle$ and

$$\begin{aligned}\tilde{g}_{\mathrm{B,min}}^{(2N)}(\mathbf{r}_1,\ldots,\mathbf{r}_N) &= g_{\mathrm{A,max}}^{(2N-2)}(\mathbf{r}_1,\mathbf{r}_1,\ldots,\mathbf{r}_{N-1},\mathbf{r}_{N-1})\,g_{\mathrm{A,max}}^{(2)}(\mathbf{r}_N,\mathbf{r}_N) \\ &= \frac{\left(P^2+3\right)(2N-2)!}{P\cdot 2^{2N}}\left[(1+P)^{2N-1}-(1-P)^{2N-1}\right],\end{aligned} \tag{A.21}$$

$$\begin{aligned}\tilde{g}_{\mathrm{B,max}}^{(2N)}(\mathbf{r}_1,\ldots,\mathbf{r}_N) &= \tilde{g}_{\mathrm{A,max}}^{(2N)}(\mathbf{r}_1,\ldots,\mathbf{r}_N) \\ &= \frac{(2N)!}{P\cdot 2^{2N+1}}\left[(1+P)^{2N+1}-(1-P)^{2N+1}\right].\end{aligned} \tag{A.22}$$

A.3 Algorithm for an arbitrary order electromagnetic intensity correlation

In principle, equations (2.27) and (A.5) can be used to obtain an arbitrary order, fully general intensity correlation given by traces of the CSDMs between the different electromagnetic fields in the system. [As is done for the double- and triple-intensity cases in equations (2.28) and (2.29), respectively.]

To cope with the increasingly complex intensity correlations of higher orders, an algorithm is introduced to automate the process. In the following, we introduce the mathematics and algorithms needed to create the normalised ICFs $g^{(N)}$ and $\tilde{g}^{(2N)}$, beginning with calculating how many correlation parameters they depend on.

Correlation coefficients Let us consider an Nth-order intensity correlation. Using Gaussian statistics, the resulting ICF will depend on the field correlations between the N fields corresponding to the intensities. If there are only two intensities, then there is only one correlation between the two fields. Given n intensities, adding one more intensity will result in n more correlations between the new field and the n previous fields. Using mathematical induction we can show that for the Nth order, the amount of different correlations is equal to $\triangle(N-1)$, where $\triangle(i) \equiv i(i+1)/2$ denotes the ith triangular number.

For case A the normalised correlations are all 0 at the minimum and 1 at the maximum. In case B the $N-1$ correlations between the test arm and the reference arms give 0 and 1 at the minimum and maximum, respectively. The identical reference arms are always fully correlated and give the remaining $\triangle(N-2)$ correlation coefficients the value 1 at both extrema.

The amount and values of the correlation coefficients for a given order are shown in table A.2.

	Maximum	Minimum of case A		Minimum of case B	
n	# of 1s	# of 0s	# of 1s	# of 0s	# of 1s
2	1	1	0	1	0
3	3	3	0	2	1
4	6	6	0	3	3
5	10	10	0	4	6
N	$\triangle(N-1)$	$\triangle(N-1)$	0	$N-1$	$\triangle(N-2)$

Table A.2. Amount and values of the correlation coefficients. For the order n (first column) all the correlation coefficients are 1 at the maximum. Thus the second column shows the total amount of correlation coefficients. The remaining columns show the amount of correlation coefficients which obtain the values 0 and 1 at the minimum for cases A and B. The symbol $\triangle(i)$ is used to denote the ith triangular number.

Breaking down the normalised intensity correlation function Using the Nth-order ICF given by equation (2.27) as a starting point for our analysis, we rearrange the summations performed over the $N!$ permutations and those performed over all the polarisation components $i_1, \ldots, i_N \in \{x, y\}$ of all the

different fields. For each permutation, the terms can be rearranged so that we have 1–N independent summations with 1–N different fields permuted within the square brackets. The amount of independent summations with square brackets and the amount of fields within each square bracket changes for each permutation, but the total amount of fields stays at N for each permutation.

For a given permutation we have

$$\begin{aligned}
&\sum_{i_1,\ldots,i_N\in\{x,y\}} \left\langle E^*_{i_1,1}\underline{E_{i_1,1}}\right\rangle \cdots \left\langle E^*_{i_N,N}\underline{E_{i_N,N}}\right\rangle \\
&= \left[\sum_{i_1,\ldots,i_r\in\{x,y\}} \left\langle E^*_{i_1,1}\underline{E_{i_1,1}}\right\rangle \cdots \left\langle E^*_{i_r,r}\underline{E_{i_r,r}}\right\rangle\right] \cdots \\
&\times \left[\sum_{i_s,\ldots,i_N\in\{x,y\}} \left\langle E^*_{i_s,s}\underline{E_{i_s,s}}\right\rangle \cdots \left\langle E^*_{i_N,N}\underline{E_{i_N,N}}\right\rangle\right]
\end{aligned} \tag{A.23}$$

where the square brackets and the underlined fields within the square brackets are in an order corresponding to what is given by the permutation in the first row of the equation.

Normalising the Nth-order ICF presented in equation (2.27) and then using equations (A.5) and (A.23), we obtain

$$g^{(N)} = \sum_{N!} \frac{\operatorname{tr}\left[\mathbf{W}_{1\underline{1}}\cdots\mathbf{W}_{r\underline{r}}\right]}{\operatorname{tr}\mathbf{W}_{11}\cdots\operatorname{tr}\mathbf{W}_{rr}} \cdots \frac{\operatorname{tr}\left[\mathbf{W}_{s\underline{s}}\cdots\mathbf{W}_{N\underline{N}}\right]}{\operatorname{tr}\mathbf{W}_{ss}\cdots\operatorname{tr}\mathbf{W}_{NN}}, \tag{A.24}$$

where, similarly to equation (A.23), the underlined indices are permuted within each square bracket term corresponding to that specific permutation in the sum. Assuming equation (4.1) holds, and using equations (2.23) and (4.4) we obtain the form

$$g^{(N)} = \sum_{N!} T(P,j)\cdots T(P,k)\left[\hat{w}_{1\underline{1}}\cdots\hat{w}_{r\underline{r}}\right]\cdots\left[\hat{w}_{s\underline{s}}\cdots\hat{w}_{N\underline{N}}\right], \tag{A.25}$$

where j and k are the number of correlation coefficients in the first and last square brackets, respectively, and the underlined indices are permuted within the square brackets as in equation (A.24).

Given any single permutation in the summation over $N!$ terms, the form of equation (A.25) is convenient to compute the weight of that term in the sum for a given value of the DoP and the correlation coefficients. Next we introduce an algorithm to generate each term in the summation.

Helper algorithm for finding closed loops in permutations To begin, we present algorithm 1, which is used to find a closed loop within the given permutation $p \in \mathrm{Perms}_N$. Perms_N is the set containing all possible permutations (orders) of the numbers in Range_N, where Range_N is a set containing

Algorithm 1 Recursive procedure for obtaining $p_j(i) \leftarrow p[\cdots p[i]\cdots]$. The symbolic values given by this procedure are listed in the last column of table A.3. This procedure is used in algorithm 2 to find closed loops in a given permutation p.

```
1: procedure p_j(i)
2:     if j = 0 then
3:         p_0(i) ← i
4:     else
5:         p_j(i) ← p[p_{j−1}(i)]
```

all positive integers up to N. For example, $p = [2, 3, 1, 4]$ is a permutation in Range_4 and it contains two closed loops: a third-order loop $1 \to 3 \to 2 \to 1$ and a first-order loop $4 \to 4$.

The procedure $p_j(i)$ is used to conveniently find a jth-order loop in a given p. For instance, in our example, shown in more detail in table A.3, the results $p_3(1) = 1$ and $p_1(4) = 4$ indicate that there is a third-order loop starting at $p[1]$ and a first-order loop starting at $p[4]$. The values of $p_1(1)$, $p_2(1)$ and $p_3(1)$ tell us which numbers in p are involved in the third-order permutation.

Thus, more generally, finding $p_j(i) = i$ is an indication of a jth-order closed loop in a given $p \in \text{Perms}_N$ and $p_1(i), \ldots, p_j(i)$ are its members. Comparing to our original problem related to equation (A.25), finding $p_j(1) = 1$ and $p_1(1), \ldots, p_j(1)$ is equivalent to finding that $T(P, j) \cdot [\hat{w}_{1\underline{1}} \cdots \hat{w}_{\underline{jj}}] = T(P, j) \cdot \hat{w}_{1p_1(1)} \cdots \hat{w}_{p_{j-1}(1)p_j(1)}$.

j	$p_j(1)$	$p_j(2)$	$p_j(3)$	$p_j(4)$	value given to $p_j(i)$
0	1	2	3	4	$p_0(i) \leftarrow i$
1	3	1	2	4	$p_1(i) \leftarrow p[i]$
2	2	3	1	4	$p_2(i) \leftarrow p[p[i]]$
3	1	2	3	4	$p_3(i) \leftarrow p[p[p[i]]]$
j	$p[p_{j-1}(i)]$			4	$p_j(i) \leftarrow p[\cdots p[i]\cdots]$

Table A.3. An example permutation $p = [2, 3, 1, 4]$ is examined. $p[i]$ indicates the ith integer in the permutation p. The first column indicates the value of the parameter j examined on each row. The columns two to five contain the values given by the procedure $p_j(i)$ for $i \in \{1, 2, 3, 4\}$. The last column contains the symbolical representation of the output when the procedure $p_j(i)$ is called. From this table we can see that the permutation p contains two loops of which one is a first order loop ($4 \leftarrow p[4]$) and the other one is a third-order loop ($1 \leftarrow p[2] \leftarrow p[p[3]] \leftarrow p[p[p[1]]]$).

The algorithm to generate $g^{(N)}$ Next, in algorithm 2, we introduce the procedure $g^{(N)}$ used to find all the closed loops in each $p \in \text{Perms}_N$. We

remind the reader that all the loops are closed and that the importance of this procedure is to find the *orders* of each specific set of loops in a permutation.

Referring to algorithm 2, lines 3 to 14 are executed for each permutation p. First a new Term is created and the set R is given the value Range_N. For each *remaining* integer $i \in R$, the lines 6 to 12 are executed. For each $j \in \text{Range}_N$, the procedure $p_j(i)$ explained above and introduced in algorithm 1 is used to find out if there is a jth-order loop in the permutation. If a loop is found then the Term is multiplied by the trace multiplier $T(P, j)$ corresponding to the order of the loop and by the correlation coefficients corresponding to the elements in the loop. Before continuing, all the integers in the found loop are removed from R to prevent the procedure from finding the same loop again. On line 12, since the loop for the examined i has already been found, the procedure breaks out of the innermost for loop and continues from the next $i \in R$. At the end of examining each permutation p, on line 13, Term is added to the collection of Terms. After each permutation has been examined, the procedure returns all the Terms.

Now, with algorithm 2, we have a procedure which can create all the $N!$ different terms in the sum on the right hand side of equation (A.25) (these are given by the output of the procedure).

Algorithm 2 Procedure for generating the terms in $g^{(N)}$. Details are provided in the text.

```
1:  procedure g^(N)
2:      for p ∈ Perms_N do
3:          Term ← 1
4:          R ← Range_N
5:          for i ∈ R do
6:              for j ∈ Range_N do
7:                  if p_j(i) = i then
8:                      Term ← Term · T(P, j)
9:                      Term ← Term · ŵ_{i p_1(i)} ··· ŵ_{p_{j−1}(i) p_j(i)}
10:                     for k ∈ Range_j do
11:                         R \ p_{k−1}(i)
12:                     break for loop, continue from next i ∈ R
13:         Terms ← Terms + Term
14:     return Terms
```

How to generate $\tilde{g}^{(2N)}$ In addition to $g^{(N)}$, we require $\tilde{g}^{(2N)}$, and the simplest way to obtain $\tilde{g}^{(2N)}$ is to use algorithm 2 to generate $g^{(2N)}$ and then replace $\hat{w}_{ij}$

with $\hat{w}_{m_i m_j}$, where m_α is the smallest integer to satisfy the congruence $\alpha \equiv^* m_\alpha \mod N$ for $\alpha \in \{i, j\}$. In practice, this means that $m_\alpha = \alpha$ when $\alpha \leq N$ and $m_\alpha = \alpha - N$ when $\alpha > N$.

It is important to note that we can not simply replace the numbers in the permutations with those that satisfy the congruence $\alpha \equiv^* m_\alpha \mod N$ before applying algorithm 2, since in this case the trace multipliers will be calculated incorrectly, although the correlation coefficients would be correctly calculated.

Conclusions Now, in addition to having all the means necessary to produce $g^{(N)}_{\Omega,\text{ext}}$ and $\tilde{g}^{(2N)}_{\Omega,\text{ext}}$, $\Omega \in \{\text{A}, \text{B}\}$ and $\text{ext} \in \{\min, \max\}$ for the image quality analysis in chapter 4, we have a robust algorithm that can be used to generate the values of the normalised ICF in almost any case applicable to correlation imaging. The main restrictions are the computational time and memory available, the compliance with equation (4.1) and the imagination of the researcher. During a practical implementation of the algorithms, it was noticed that the computational resources started to reach their limits when calculating $\tilde{g}^{(2N)}$ for $N = 5$ while using a typical desktop machine built in 2014.

Errata for publications

There is a miscalculation in equation (30) in [15]. The correct result is given by equation (4.14b), that is, equation (30) in [15] should read as

$$V_{\mathrm{G}}^{(3)} = \frac{5P^2 + 3}{6P^2 + 6}.$$

Bibliography

[1] J. W. Goodman, *Introduction to Fourier Optics*, 3rd ed. (Roberts & Company, 2005).

[2] T. Pittman, Y. Shih, D. Strekalov and A. Sergienko, "Optical imaging by means of two-photon quantum entanglement," *Phys. Rev. A* **52**, R3429 (1995).

[3] D. Strekalov, A. Sergienko, D. Klyshko and Y. Shih, "Observation of two-photon "ghost" interference and diffraction," *Phys. Rev. Lett.* **74**, 3600 (1995).

[4] R. Bennink, S. Bentley and R. Boyd, "Two-photon coincidence imaging with a classical source," *Phys. Rev. Lett.* **89**, 113601 (2002).

[5] A. Gatti, E. Brambilla, M. Bache and L. Lugiato, "Correlated imaging, quantum and classical," *Phys. Rev. A* **70**, 013802 (2004).

[6] A. Gatti, E. Brambilla, M. Bache and L. Lugiato, "Ghost imaging with thermal light: Comparing entanglement and classical correlation," *Phys. Rev. Lett.* **93**, 093602 (2004).

[7] F. Ferri, D. Magatti, A. Gatti, M. Bache, E. Brambilla and L. Lugiato, "High-resolution ghost image and ghost diffraction experiments with thermal light," *Phys. Rev. Lett.* **94**, 183602 (2005).

[8] D.-Z. Cao, J. Xiong, S.-H. Zhang, L.-F. Lin, L. Gao and K. Wang, "Enhancing visibility and resolution in *n*th-order intensity correlation of thermal light," *Appl. Phys. Lett.* **92**, 201102 (2008).

[9] L. Mandel and E. Wolf, *Optical Coherence and Quantum Optics* (Cambridge University, 1995).

[10] B. E. A. Saleh and M. C. Teich, *Fundamentals of Photonics*, 2nd ed. (Wiley, 2007).

[11] H.-C. Liu, D.-S. Guan, L. Li, S.-H. Zhang and J. Xiong, "The impact of light polarization on imaging visibility of *n*th-order intensity correlation with thermal light," *Opt. Commun.* **283**, 405 (2010).

[12] T. Shirai, H. Kellock, T. Setälä and A. T. Friberg, "Visibility in ghost imaging with classical partially polarized electromagnetic beams," *Opt. Lett.* **36**, 2880 (2011).

[13] T. Shirai, H. Kellock, T. Setälä and A. T. Friberg, "Visibility in ghost imaging with partially polarized beams," in *9th Euro-American Workshop on Information Optics,* Helsinki, Finland (2011); IEEE Xplore doi: 10.1109/WIO.2010.5582500, edited by P. O. T. X. A. C. O. T. F. P. SOCIETY and T. S. N. P. MEETING, p. 361 (2011).

[14] H. Kellock, T. Setälä, T. Shirai and A. T. Friberg, "Higher-order ghost imaging with partially polarized classical light," *Proc. SPIE* **8171**, 81710Q (2011).

[15] H. Kellock, T. Setälä, T. Shirai and A. T. Friberg, "Image quality in double- and triple-intensity ghost imaging with classical partially polarized light," *J. Opt. Soc. Am. A* **29**, 2459 (2012).

[16] T. Shirai, H. Kellock, T. Setälä and A. T. Friberg, "Imaging through an aberrating medium with classical ghost diffraction," *J. Opt. Soc. Am. A* **29**, 1288 (2012).

[17] H. Kellock, T. Setälä, A. T. Friberg and T. Shirai, "Polarimetry by classical ghost diffraction," *Journal of Optics* **16**, 055702 (2014).

[18] J. D. Jackson, *Classical Electrodynamics*, 3rd ed. (Wiley, 1998).

[19] G. B. Arfken and H. J. Weber, *Mathematical Methods for Physicists*, 6th ed. (Elsevier, 2005).

[20] J. W. Goodman, *Statistical Optics* (Wiley, 1985).

[21] A. Gatti, M. Bache, D. Magatti, E. Brambilla, F. Ferri and L. A. Lugiato, "Coherent imaging with pseudo-thermal incoherent light," *J. Mod. Opt.* **53**, 739 (2006).

[22] J. W. Goodman, *Introduction to Fourier Optics*, 2nd ed. (McGraw-Hill, 1996).

[23] S. Hassani, *Mathematical Methods: For Students of Physics and Related Fields* (Springer, 2000).

[24] A. Starikov and E. Wolf, "Coherent-mode representation of gaussian schell-model sources and of their radiation fields," *J. Opt. Soc. Am.* **72**, 923 (1982).

[25] Y. Cai and S.-Y. Zhu, "Ghost interference with partially coherent radiation," *Opt. Lett.* **29**, 2716 (2004).

[26] H. Kellock, *Temporal ghost imaging by triple-intensity correlation of random classical fields*, Master's thesis, University of Helsinki (2011).

[27] J. Cheng, "Transfer functions in lensless ghost-imaging systems," *Phys. Rev. A* **78**, 043823 (2008).

[28] J. Cheng and S. Han, "Incoherent coincidence imaging and its applicability in x-ray diffraction," *Phys. Rev. Lett.* **92**, 093903 (2004).

[29] M. Zhang, Q. Wei, X. Shen, Y. Liu, H. Liu, J. Cheng and S. Han, "Lensless Fourier-transform ghost imaging with classical incoherent light," *Phys. Rev. A* **75**, 021803 (2007).

[30] H. Liu, X. Shen, D.-M. Zhu and S. Han, "Fourier-transform ghost imaging with pure far-field correlated thermal light," *Physical Review A* **76**, 053808 (2007).

[31] I. Agafonov, M. Chekhova, T. S. Iskhakov and L.-A. Wu, "High-visibility intensity interference and ghost imaging with pseudo-thermal light," *J. Mod. Opt.* **56**, 422 (2009).

[32] F. Ferri, D. Magatti, L. Lugiato and A. Gatti, "Differential ghost imaging," *Phys. Rev. Lett.* **104**, 253603 (2010).

[33] K. W. C. Chan, M. N. O'Sullivan and R. W. Boyd, "High-order thermal ghost imaging," *Opt. Lett.* **34**, 3343 (2009).

[34] X.-H. Chen, I. N. Agafonov, K.-H. Luo, Q. Liu, R. Xian, M. V. Chekhova and L.-A. Wu, "High-visibility, high-order lensless ghost imaging with thermal light," *Opt. Lett.* **35**, 1166 (2010).

[35] H.-C. Liu and J. Xiong, "Properties of high-order ghost imaging with natural light," *J. Opt. Soc. Am. A* **30**, 956 (2013).

[36] J. Li, D. Yang, B. Luo, G. Wu, L. Yin and H. Guo, "Image quality recovery in binary ghost imaging by adding random noise," *Opt. Lett.* **42**, 1640 (2017).

[37] A. Gatti, E. Brambilla and L. Lugiato, "Quantum imaging," in *Progress in Optics*, edited by E. Wolf, vol. 51, pp. 251–348 (Elsevier, 2008).

[38] Y.-C. Liu and L.-M. Kuang, "A theoretical scheme of thermal-light ghost imaging by nth-order intensity correlation," ArXiv:0903.5015 (2009).

[39] K. W. C. Chan, M. N. O'Sullivan and R. W. Boyd, "Optimization of thermal ghost imaging: high-order correlations vs. background subtraction," *Opt. Express* **18**, 5562 (2010).

[40] G. Brida, M. Chekhova, G. Fornaro, M. Genovese, E. Lopaeva and I. Berchera, "Systematic analysis of signal-to-noise ratio in bipartite ghost imaging with classical and quantum light," *Phys. Rev. A* **83**, 063807 (2011).